Evidence for Dark Matter Contraction and a Salpeter Initial Mass Function in a Massive Early-type Galaxy

Sonnenfeld, A.; Treu, T.; Gavazzi, R.; Marshall, P. J.; Auger, M. W.; Suyu, S. H.; Koopmans, L. V. E.; Bolton, A. S.

Published in:
Astrophysical Journal

DOI:
10.1088/0004-637X/752/2/163

Publication date:
2012

The Astrophysical Journal, 752:163 (17pp), 2012 June 20 doi:10.1088/0004-637X/752/2/163

EVIDENCE FOR DARK MATTER CONTRACTION AND A SALPETER INITIAL MASS FUNCTION IN A MASSIVE EARLY-TYPE GALAXY

A. Sonnenfeld[1], T. Treu[1], R. Gavazzi[2], P. J. Marshall[3], M. W. Auger[1,4], S. H. Suyu[1], L. V. E. Koopmans[5], and A. S. Bolton[6]
[1] Department of Physics, University of California, Santa Barbara, CA 93106, USA; sonnen@physics.ucsb.edu
[2] Institut d'Astrophysique de Paris, UMR7095 CNRS-Université Pierre et Marie Curie, 98bis bd Arago, 75014 Paris, France
[3] Department of Physics, University of Oxford, Keble Road, Oxford OX1 3RH, UK
[4] Institute of Astronomy, University of Cambridge, Madingley Road, Cambridge CB3 0HA, UK
[5] Kapteyn Institute, University of Groningen, P.O. Box 800, 9700 AV Groningen, The Netherlands
[6] Department of Physics and Astronomy, University of Utah, Salt Lake City, UT 84112, USA
Received 2011 November 15; accepted 2012 April 18; published 2012 June 6

ABSTRACT

Stars and dark matter account for most of the mass of early-type galaxies, but uncertainties in the stellar population and the dark matter profile make it challenging to distinguish between the two components. Nevertheless, precise observations of stellar and dark matter are extremely valuable for testing the many models of structure formation and evolution. We present a measurement of the stellar mass and inner slope of the dark matter halo of a massive early-type galaxy at $z = 0.222$. The galaxy is the foreground deflector of the double Einstein ring gravitational lens system SDSSJ0946+1006, also known as the "Jackpot." By combining the tools of lensing and dynamics we first constrain the mean slope of the total mass density profile ($\rho_{\rm tot} \propto r^{-\gamma'}$) within the radius of the outer ring to be $\gamma' = 1.98 \pm 0.02 \pm 0.01$. Then we obtain a bulge-halo decomposition, assuming a power-law form for the dark matter halo. Our analysis yields $\gamma_{\rm DM} = 1.7 \pm 0.2$ for the inner slope of the dark matter profile, in agreement with theoretical findings on the distribution of dark matter in ellipticals, and a stellar mass from lensing and dynamics $M_*^{\rm LD} = 5.5^{+0.4}_{-1.3} \times 10^{11}\,M_\odot$. By comparing this measurement with stellar masses inferred from stellar population synthesis fitting we find that a Salpeter initial mass function (IMF) provides a good description of the stellar population of the lens while the probability of the IMF being heavier than Chabrier is 95%. Our data suggest that growth by accretion of small systems from a compact red nugget is a plausible formation scenario for this object.

Key words: dark matter – galaxies: elliptical and lenticular, cD – galaxies: structure – gravitational lensing: strong

Online-only material: color figures

1. INTRODUCTION

What are the main physical processes that shape early-type galaxies (ETGs)? Understanding the formation and evolution of ETGs is a fundamental piece in the cosmological puzzle. Any model that aims at providing a description of the universe as a whole must be able to reproduce the observed characteristics of these objects.

ETGs are observed to hold tight scaling relations, such as the fundamental plane (Dressler et al. 1987; Djorgovski & Davis 1987) and the correlation between the mass of the central black hole and global galactic properties (Ferrarese & Merritt 2000; Gebhardt et al. 2000; Marconi & Hunt 2003). The inner density profile of their total mass is measured to be very close to isothermal, in the so-called bulge-halo conspiracy (Treu & Koopmans 2004; Koopmans et al. 2006, 2009; Auger et al. 2010a). Moreover, they appear to undergo a significant evolution in size, from being very compact in the early ($z \sim 2$) universe to the more diffuse objects that we observe at more recent times (van der Wel et al. 2008; van Dokkum et al. 2008; Newman et al. 2010). Finally, studies of massive ETGs seem to favor a heavier stellar initial mass function (IMF; Grillo et al. 2009; Treu et al. 2010; van Dokkum & Conroy 2010, 2011; Auger et al. 2010b; Spiniello et al. 2011) than for spiral galaxies (Bell & de Jong 2001; Dutton et al. 2011; Suyu et al. 2012).

These characteristics should reflect a common mechanism that drives ETGs toward the tight relations observed at low redshifts ($z \lesssim 0.3$) during their formation and evolution. Mergers with other galaxies are likely to be one of the key processes in the history of ETGs. Mergers are believed to be at the basis of the formation (Kormendy & Sanders 1992; Hernquist 1992; Shier & Fischer 1998), to be involved in the black hole scaling relation (Haehnelt & Kauffmann 2000; Peng 2007) and to drive the size evolution (Hopkins et al. 2009a; Oser et al. 2012) of ETGs. However, the picture is complicated by the many physical processes that are present during the evolution of galaxies, such as gas cooling, feedback from stars, and active galactic nuclei (AGNs). Moreover, an important fraction of the mass of ETGs is accounted for by dark matter (DM; Bertin et al. 1994; Franx et al. 1994; Gerhard et al. 2001; Treu & Koopmans 2004; Barnabè et al. 2011) whose nature is still unknown. Understanding the interplay of baryonic and DM and how they act to produce the observed structural characteristics is essential to comprehend the evolution of ETGs, but is today a challenging task.

Theoretical models and simulations with a variety of physical ingredients have been set up to try to reproduce the observables of ETGs (Gustafsson et al. 2006; Hopkins et al. 2010; Schaye et al. 2010; Duffy et al. 2010). Although simulations seem to be able to capture the general characteristics of ETGs (e.g., Hopkins et al. 2009b; Ciotti et al. 2010), quantitatively matching the entire set of observables proved to be difficult, often requiring an ad hoc tuning of the model parameters (Nipoti et al. 2009; Hopkins et al. 2010). For example, Duffy et al. (2010) explored a variety of aspects of baryonic physics such as gas cooling, feedback from stars, and AGNs, finding that on the one

hand the observed inner slopes of massive ETGs are reproduced if the feedback is weak, but on the other hand a strong feedback is needed to match the measured stellar masses.

Improving the quality of the observation of ETGs and introducing more constraints can help us to discriminate between the wealth of currently viable scenarios for their history. Two characteristics of ETGs in particular are still not known with sufficient precision and leave room for significant improvement in their observational determination: the stellar mass and the density profile of the DM halo. The stellar mass is degenerate with the stellar IMF with respect to constraints from the integrated light distribution and colors. Breaking this degeneracy can help in determining the star formation history and the content of the baryonic mass in ETGs. The density profile of the DM distribution is sensitive to the physical processes that take place during the formation and evolution of ETGs. Therefore, measuring the profile of DM halos in ETGs is a powerful means for testing the various theoretical models.

Part of the difficulty in comparing simulations with observations are, of course, due to the fact that DM, which accounts for a significant fraction of the mass of a typical galaxy, is not directly observable. Gravitational lensing is, in this aspect, a very powerful tool, being sensitive to the gravitational pull of matter independently on its interaction with light (e.g., Treu 2010 and references therein).

Lensing surveys indeed played a crucial role in uncovering physical characteristics of ETGs, such as their average density profile and DM fraction (Koopmans et al. 2006, 2009; Auger et al. 2010a; Barnabè et al. 2011) or the IMF of their stellar population (Grillo et al. 2009; Treu et al. 2010; Auger et al. 2010b). Measurements of the inner slope of a DM halo have so far been obtained for a few cluster lenses (e.g., Sand et al. 2008; Newman et al. 2009), for which constraints from multiple lensed sources are available. For typical ETG strong lenses, however, there are residual degeneracies between anisotropy, stellar mass-to-light ratio, and inner slope of the DM halo, and therefore the constraints are weak (Koopmans & Treu 2003; Treu & Koopmans 2004). For this reason, previous studies have adopted theoretically motivated mass density profiles for the DM halo (Treu et al. 2010; Auger et al. 2010b), rather than free power laws.

Here we present a detailed study of an ETG at redshift $z = 0.222$. The galaxy is the strong gravitational lens of the system SDSSJ0946+1006, part of the SLACS sample (Bolton et al. 2004). This ETG is special in that it lenses two sources at different redshifts, creating two nearly complete Einstein rings of different radii. For this reason, the system is also referred to as the "Jackpot." The first lensed source is at redshift $z_{s1} = 0.609$, while there is no spectroscopic measurement of the redshift of the second ring. Thanks to the presence of the two rings, this system provides more information than typical gravitational lenses, despite the lack of the second source redshift. A first study of SDSSJ0946+1006 was carried out by Gavazzi et al. (2008, hereafter Paper VI). An independent lensing analysis of this system was performed by Vegetti et al. (2010), which led to the discovery of a small satellite with no visible counterpart. Here we include new high-quality photometry obtained with the *Hubble Space Telescope* (*HST*) and new deep and spatially resolved spectroscopy obtained at the Keck Telescope. The goal of our study is to separate the contribution of dark and stellar matter to the total mass of the lens, making as few assumptions as possible about the density profile of the DM halo. This task is achieved by combining lensing and dynamics information.

Table 1
Summary of the *HST* Observations

Instrument	Filter	Exp. Time	$N_{\rm exp}$	Date
WFC3 IR	F160W	2397 s	4	2009 Dec 9
ACS	F814W	2096 s	4	2006 Nov 3
WFPC2	F606W	4400 s	4	2009 Dec 18
WFC3 UVIS	F438W	2520 s	4	2010 Mar 20
WFC3 UVIS	F336W	5772 s	4	2010 Mar 20

Unlike typical ETG lenses, the wealth of information provided by this system allows us to determine both the mass of the stellar bulge and the inner slope of the DM halo. Thanks to the multiband *HST* photometry we are able to obtain a photometric redshift of the outer ring, which is necessary for improving the constraints from the lensing data, and to infer stellar masses from stellar population synthesis (SPS) fitting. The comparison between this measurement of the stellar mass and the one obtained through lensing and dynamics allows us to constrain the IMF of the stars in the lens. This is the most robust measurement of the inner slope of the DM halo and IMF of an isolated massive ETG.

The structure of this paper is the following. In Sections 2 and 3 we describe the new photometric and spectroscopic data, respectively. Our measurement of the photometric redshift of the outer ring is presented in Section 4. In Section 5 we describe measurements of the stellar mass of the lens from SPS fitting. Section 6 describes a lensing and dynamics model assuming a power-law density profile for the total density profile of the lens. In Section 7 we present the bulge-halo decomposition of the lens. We discuss our results in Section 8 and summarize in Section 9.

Throughout the paper we assume the following values for the cosmological parameters $H_0 = 70\,{\rm km\,s^{-1}\,Mpc^{-1}}$, $\Omega_M = 0.3$, $\Omega_\Lambda = 0.7$. Magnitudes are expressed in the AB system, images are north-up and position angles are in degrees east of north. In showing our results we display posterior probability distribution functions (PDFs) in multiple projections wherever possible, but when giving a point estimate of an inferred parameter we quote the position of the peak of its one-dimensional marginalized distribution, with uncertainties defined by the 68% credible region.

2. MULTICOLOR *HST* PHOTOMETRY

We present *HST* images of the lens system SDSSJ0946+1006 in five different bands. In Paper VI we reported results based on an ACS F814W image only. Images in WFPC2 F606W and WFC3-IR F160W (Cycle 16, Program 11202, PI: Koopmans) were available for Paper IX (Auger et al. 2009). In addition to those data, we now have WFC3 images in F438W and F336W bands (Cycle 17, Program 11701, PI: Treu). Table 1 summarizes the observations. This section describes the data reduction process (Section 2.1) and the photometric properties we derived for the lens galaxy (Section 2.2). For conciseness, we sometimes refer to the F160W, F814W, F606W, F438W, and F336W bands as H, I, V, B, and U, respectively. A color composite image of the lens system is shown in Figure 1.

2.1. Data Reduction

The data are treated with the standard *HST* reduction pipeline. For each image, frames are co-added and resampled in a uniform pixel scale using the software MULTIDRIZZLE (Fruchter et al.

Table 2
Lens Light Distribution: Double-Sérsic Model

Component	m_{F814W} (mag)	r_{eff} (arcsec)	n	q	P.A. (deg)	$\langle SB \rangle_{e,F814W}$ (mag arcsec^{-2})
1	18.38 ± 0.20	0.50 ± 0.10	2.34 ± 0.50	0.79 ± 0.10	63.0 ± 1.0	18.87 ± 0.10
2	17.44 ± 0.10	4.46 ± 0.50	1.60 ± 0.50	0.64 ± 0.10	-23.4 ± 1.0	22.68 ± 0.20

Notes. Best-fit parameters for the double-Sérsic model surface brightness profile of the main lens: magnitude in the F814W band, effective radius, Sérsic index (n), axis ratio (q), position angle of the major axis (east of north), and effective surface brightness. Each line refers to one of the Sérsic components of the model. The errors represent the typical range of values for the parameters allowed by the model. These errors are correlated: for example, an increase in the value of the Sérsic index n results in a change of the effective radius to fit the observed slope in surface brightness.

Table 3
Lens Light Distribution: Double-tPIEMD Model

Component	m_{F814W} (mag)	r_c (arcsec)	r_t (arcsec)	q	P.A. (deg)	$\langle SB \rangle_{e,F814W}$ (mag arcsec^{-2})
1	18.75 ± 0.20	0.066 ± 0.010	0.50 ± 0.05	0.66 ± 0.10	63.0 ± 1.0	19.24 ± 0.10
2	17.15 ± 0.10	0.082 ± 0.010	6.05 ± 0.10	0.71 ± 0.10	-24.3 ± 1.0	22.48 ± 0.20

Notes. Best-fit parameters for the double-tPIEMD model surface brightness profile of the main lens: magnitude in the F814W band, core radius (r_c), truncation radius (r_t), axis ratio (q), position angle of the major axis (east of north), and effective surface brightness.

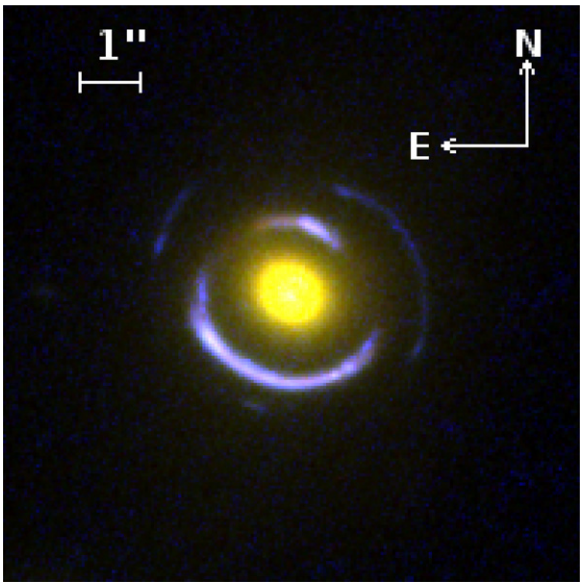

Figure 1. Gravitational lens system SDSSJ0946+1006 in a combination of F814W, F606W, and F336W *HST* images.
(A color version of this figure is available in the online journal.)

2009). Pixel sizes are 0.″10 for the F160W image, 0.″050 for the F814W and F606W images, and 0.″0396 for the F438W and F336W images. The images are then brought to the same orientation and 0.″050 pixel scale by using the software SWARP (Bertin et al. 2002). The point-spread function (PSF) of each image is estimated from stars in the field.

2.2. Lens Galaxy Properties

The brightness distribution of the main lens galaxy is first obtained by fitting Sérsic profiles to the data. This task is achieved with the software SPASMOID, developed by M. W. Auger and described by Bennert et al. (2011). SPASMOID fits the data in all the bands simultaneously with a unique model, determining total magnitude and colors of the galaxy at once. By using a single Sérsic component we find a best-fit profile described by a Sérsic index $n = 6.0$, axis ratio $q = 0.95$, and effective radius $r_{eff} = 2.''93$. However, the residuals left by this single-component fit are rather large. Consequently, we add a second component, allowing for the position angle of the major axes of the two profiles to be different but imposing a common centroid. In the fitting process, the light from the rings is masked out manually. This procedure gives robust estimates of the colors of the lens, rather independent from the model adopted to describe the data. Color information will be used in Section 5 to constrain the stellar population. In Figure 2 we show the images of the system in the five bands, before and after subtracting the main lens. Residuals are on the order of a few percent in the F814W-band image. Table 2 reports the best-fit structural parameters of the model, while the best-fit colors are given in Table 4. It is worth pointing out that the major axes of the two components are almost perpendicular, and that the mean surface brightness within the effective radius of component 1 is a factor $\sim$30 larger than that of component 2. The measured magnitude in the F814W band is consistent with the value reported by Gavazzi et al. (2008) for the same object.

Table 4
Colors of the Lens Galaxy

Color	Component 1	Component 2	Global
$I - H$	1.16 ± 0.05	0.86 ± 0.05	0.96 ± 0.05
$V - I$	0.81 ± 0.05	0.96 ± 0.05	0.91 ± 0.05
$B - V$	2.36 ± 0.20	1.52 ± 0.05	1.73 ± 0.05
$U - B$	2.30 ± 0.30	1.32 ± 0.10	1.44 ± 0.10

In order to both explore model-dependent systematic errors and obtain a computationally more tractable description of the light profile for our lensing analysis, we also model the lens light with the following surface brightness distribution:

$$I(x, y) = I_c r_c \left[\frac{1}{\sqrt{r_c^2 + R^2}} - \frac{1}{\sqrt{r_t^2 + R^2}} \right], \quad (1)$$

where $R^2 \equiv x^2/q + q y^2$. This profile corresponds to a truncated pseudoisothermal elliptical mass distribution (tPIEMD) in three dimensions (3D), with r_c and r_t corresponding to the core radius and truncation radius, respectively. Note that the number of parameters of the model is the same as that of a Sérsic profile.

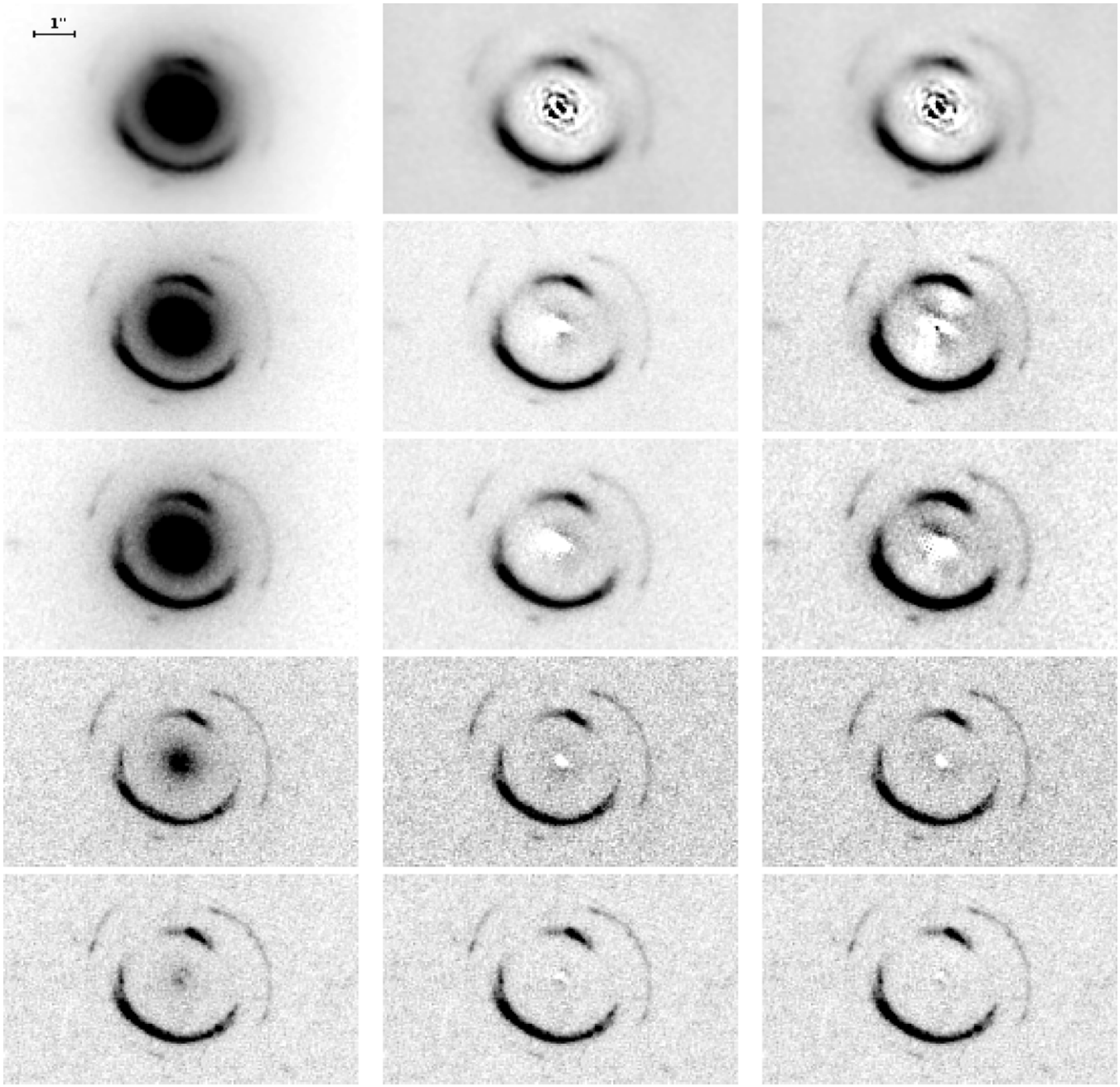

Figure 2. From top to bottom: *HST* F160W, F814W, F606W, F438W, and F336W images of the lens system SDSSJ0946+1006 before (left column) and after (middle and right column) light subtraction. Middle column: light distribution modeled as a double-Sérsic profile, with parameters given in Table 2. Right column: light distribution modeled as a double-tPIEMD profile, with parameters given in Table 3.

Two components are used, as in the Sérsic case. The best-fit parameters are reported in Table 3. Both the double-Sérsic and the double-tPIEMD profiles fit the photometry of the lens well, with residuals within the outer ring on the order of a few percent in the F814W band (see Figure 2).

The inferred total magnitude in the two models is different, but this is due to the different behavior at large radii, where there are no data. In fact, the magnitude within the inner ring is the same for the two models to within 0.01 mag and the inferred colors are consistent within the errors with those reported in Table 4.

The infrared F160W data reveal distortions in the shape of the light distribution at large radii (see Figure 3), a possible signature of tidal interactions. As previously noted by Gavazzi et al. (2008), a galaxy in the neighborhood of the lens also shows signs of a tidal interaction (see Figure 3). It is possible that the two galaxies are undergoing a merger. This deviation from a regular light profile is located far from the probed by our lensing and dynamics measurements and is therefore not a concern for the accuracy of our models. The central part appears smooth to the few percent level and it is unlikely that the ongoing interaction would have an effect on its structure, given its deep potential well. However, as we will discuss in Section 8.2 this feature provides an interesting clue to the formation mechanism of this galaxy.

Another interesting feature is revealed by the image in the F336W (U) band, as there seems to be some structure in the center of the lens (see Figure 2). The fact that this feature is

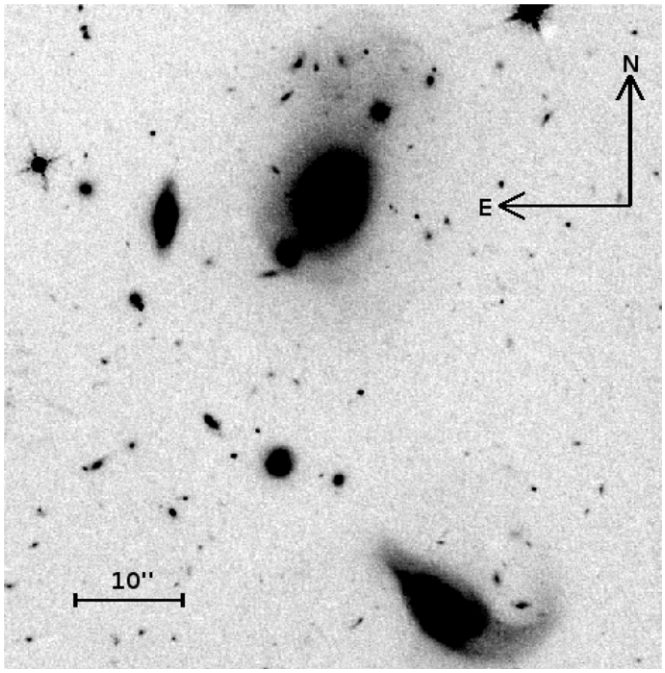

Figure 3. WFC3-IR F160W image of the lens system and its surroundings. Note the irregular shape of the faint stellar component at the outskirts of the lens galaxy (top of the image). At the bottom, a neighbor also shows signs of tidal disruption. Both these features may be the result of a close encounter between the two objects.

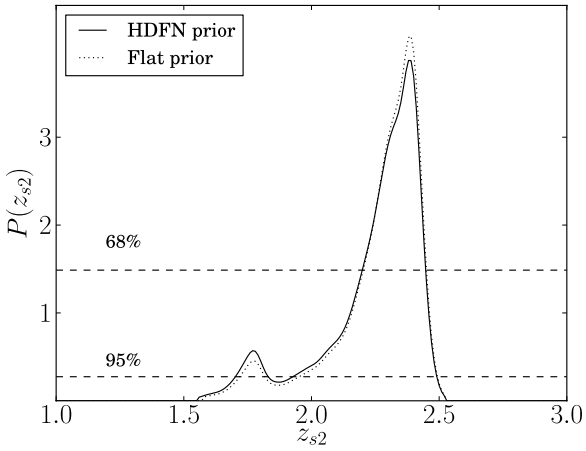

Figure 4. Solid line: posterior probability distribution function of the source redshift, as calculated with BPZ, assuming a prior on z_{s2} from Hubble Deep Field North number counts. Overplotted are the levels corresponding to 68% and 95% enclosed probability. Dotted line: posterior PDF assuming a flat prior on z_{s2}.

Table 5
AB Colors of the Outer Ring

$I - H$	0.61 ± 0.10
$V - I$	0.21 ± 0.10
$B - V$	0.15 ± 0.10
$U - B$	0.53 ± 0.10

clearly visible only in the *U* band, where the lens is fainter, may suggest that it is in fact a bluer object distinct from the central galaxy, or blue emission from an active nucleus. Alternatively, the observed detail could be the result of the presence of a dust lane that separates the light of the lens into two components at shorter wavelengths. In principle it could also be an additional image of the lensed sources.

One way to discriminate between a blue object or a dust lane is to study the position of the centroid of the lens in the different bands. A blue object would shift the centroid toward itself at bluer wavelengths, while a dust lane would remove blue light, causing the apparent centroid to move away from it. When fitting for the centroid of the lens, this latter case is observed: the centroid moves by about 1 pixel toward the south to east in the F336W and F438W bands with respect to the F814W band. This is a significant effect given the subpixel accuracy of centroiding, and it suggests that dust is most likely the cause of the observed feature in the F336W band. A more detailed discussion of the dust issue is given in Appendix A.

3. PHOTOMETRIC REDSHIFT OF THE OUTER RING

3.1. Colors of the Ring

One of the main goals of this study is to constrain better the mass distribution in the lens galaxy by obtaining a photo-z of the outer ring. This task requires a measurement of the colors of the ring. A color map of the outer ring is obtained as follows. For each pair of neighboring bands, λ_1, λ_2, we align the corresponding images and then convolve each image with the PSF of the neighboring band. In this way we obtain pairs of images with the same effective PSF, necessary to get an unbiased estimate of the color for each pixel. Global colors are then measured in the following way. For a given pair of bands, we select individual pixels with flux larger than the background by more than 2σ in both of the bands considered. We make the assumption that the source has spatially uniform colors and estimate them statistically by taking a weighted mean of the individual pixel colors. The measured values of the colors, corrected for galactic extinction, are reported in Table 5.

3.2. Measuring the Photo-z

To estimate the photometric redshift of the outer ring we make use of the software BPZ (Bayesian Photo-z; Benítez 2000). Photo-z analysis consists of fitting synthetic spectral energy distributions (SEDs) to the observed colors. BPZ works in a Bayesian framework that allows us to combine the inference with that from other pieces of information: given a prior probability distribution for the source redshift and galaxy type, BPZ calculates the probability of the source being at redshift z_{s2} given its colors $\mathbf{C}$ and magnitude m, $P(z_{s2}|\mathbf{C}, m)$. The stellar templates used for the SED fitting are described by Coe et al. (2006). The F814W magnitude is taken from Gavazzi et al. (2008), where the brightness distribution of the source was reconstructed after a lens modeling. The value adopted is therefore $m_{\mathrm{F814W}} = 27.01 \pm 0.19$.

For the redshift distribution we use a prior $P(z|m_{\mathrm{F814W}})$ suggested by Benítez (2000) and based on number counts from the Hubble Deep Field North. Figure 4 shows the redshift posterior PDF $P(z_{s2}|\mathbf{C}, m_{\mathrm{F814W}})$. The most likely redshift with 68% confidence interval is $z_{s2} = 2.41^{+0.04}_{-0.21}$. As will be shown later, this information is sufficient to put interesting constraints on the model of the lens system. We also calculated the photo-z assuming a flat prior on z_{s2}, and found a nearly identical result. Colors calculated with a different lens light subtraction, the double-Sérsic model, yield the same photo-z well within the quoted uncertainties.

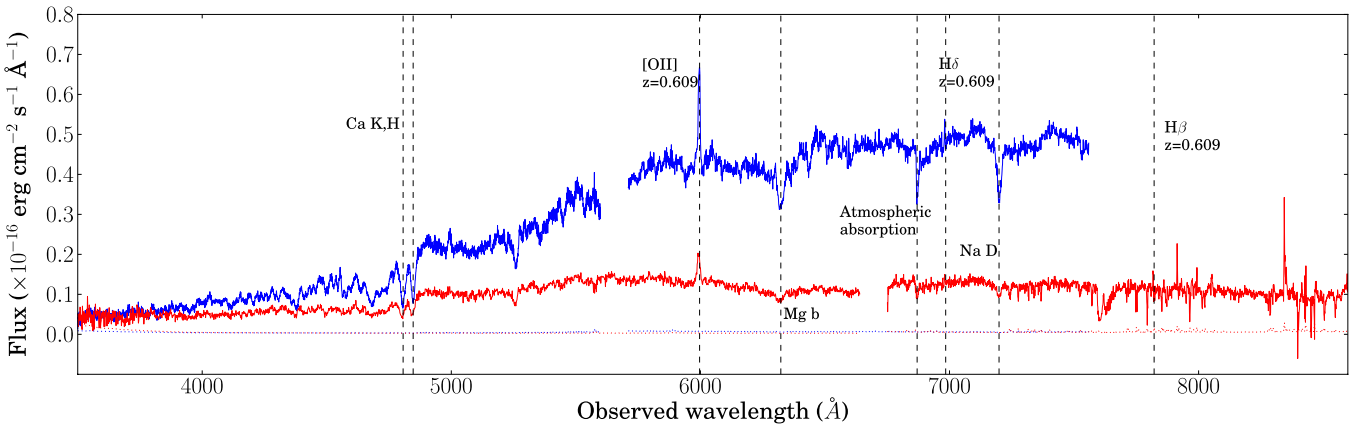

Figure 5. LRIS spectra of the Jackpot. Blue: data from the first night. Red: data from the second night. The two spectra are extracted from rectangular apertures $1'' \times 3''.36$. Dotted line: noise level.

(A color version of this figure is available in the online journal.)

Table 6
Spectroscopic Observations: Summary

Date	Exp. time	Slit width	Dichroic	Blue grism	Red grating	Red λ_c	Weather	Seeing
2006 Dec 23	16200	$1''.0$	560	600/4000	831/8200	6819 Å	Good	$0''.8$
2006 Dec 24	12600	$1''.0$	680	300/5000	831/8200	7886 Å	Good	$0''.8$

4. KECK SPECTROSCOPY

The data were collected during the nights of 2006 December 23 and 24 with the LRIS instrument at the Keck Telescope I. The original goals of the observations were to measure a velocity dispersion profile of the foreground deflector and to measure the redshift of the outer ring. The first goal was successfully achieved, while we were not able to detect any spectroscopic signature from the farthest source.

Because of the dual scope of our study, two different instrumental setups were used. The first setup, used during the first night, was optimized for a better measurement of the velocity dispersion of the deflector. The wavelength range in the red detector, the one used for the measurement of σ, was ∼5700–7600 Å, bracketing important absorption features in the rest frame of the lens at $z = 0.222$. During the second night we centered the slit on the longest arc of the outer ring, and used a setup with a broader wavelength range, up to ∼8600 Å. A summary of the observations, with specifications on the setups used, is provided in Table 6.

The spectrum of the system is shown in Figure 5. There is no evidence for the presence of emission lines from objects other than the foreground lens and the inner ring. Given our measurement of the photo-z of the outer ring, we would expect Lyα emission to fall around ∼4150 Å, but it cannot be identified in our spectrum. We can put an upper limit of $\sim 5 \times 10^{-18}$ erg cm^{-2} s^{-1} to the flux in Lyα from the source.

4.1. Velocity Dispersion

The velocity dispersion of the main lens is measured by fitting stellar templates convolved with a Gaussian velocity distribution to the observed spectrum. This operation is carried out with a Markov Chain Monte Carlo (MCMC) approach, using a code developed by M. W. Auger, and described by Suyu et al. (2010). The rest frame wavelength range used for the fit is 5100–5850 Å. For the stellar templates we used linear combinations of nine spectra from the INDO-US library, corresponding to K, G, F, and A stars. The most prominent absorption feature in the wavelength range considered is Mgb (5175 Å). However, we experienced difficulty in finding a good fit to both Mgb and the rest of the spectrum. It is known that some galaxies have enhanced magnesium features in the spectrum that are not reproduced well in standard stellar templates (Barth et al. 2002). For this reason we decided to mask the Mgb absorption line out of the fitted spectrum.

Table 7
Velocity Profile Measurements

Slit Offset (arcsec)	$\langle v \rangle$ (km s^{-1})	σ (km s^{-1})
−1.05	101 ± 21	252 ± 25
−0.84	85 ± 16	273 ± 18
−0.63	62 ± 11	263 ± 14
−0.42	30 ± 10	278 ± 12
−0.21	20 ± 10	287 ± 11
0.00	0 ± 9	287 ± 11
0.21	-22 ± 11	286 ± 11
0.42	-55 ± 12	299 ± 13
0.63	-67 ± 13	274 ± 15
0.84	-63 ± 15	272 ± 19
1.05	-94 ± 24	301 ± 25

Notes. Mean velocity and velocity dispersion profile. Apertures are $1.00 \times 0''.21$ rectangles.

With the aim of obtaining a velocity dispersion profile, we measured σ in a set of apertures. The spatial position of the apertures was determined by fitting the centroid of the trace of the lens in the two-dimensional spectra and it is accurate to $\sim 0''.02$. In Table 7 and Figure 6 we report the measured values of σ and of the mean velocity in each aperture, while in Figure 7 we show the fit in the central $0''.42$ as an example. There is evidence for some rotation, with $v_{\rm rot}^2 \ll \sigma^2$.

5. STELLAR MASSES

Here we present a measurement of the stellar mass of the foreground lens galaxy. The procedure adopted is the following:

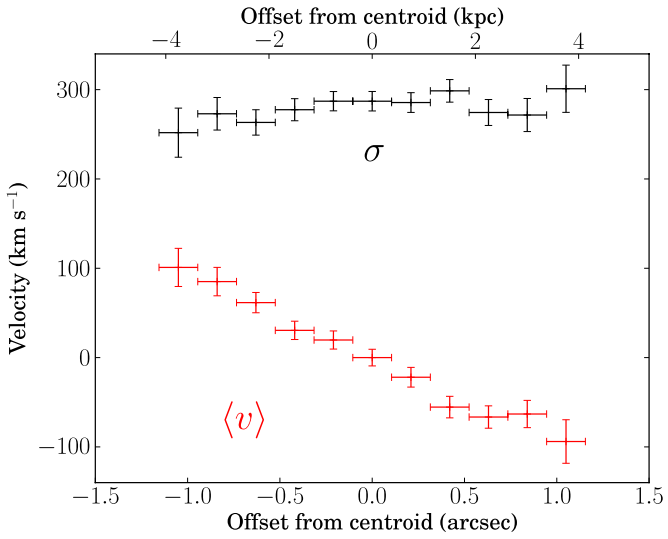

Figure 6. Mean velocity and velocity dispersion profiles of the main lens within 1.″15 from the centroid.

(A color version of this figure is available in the online journal.)

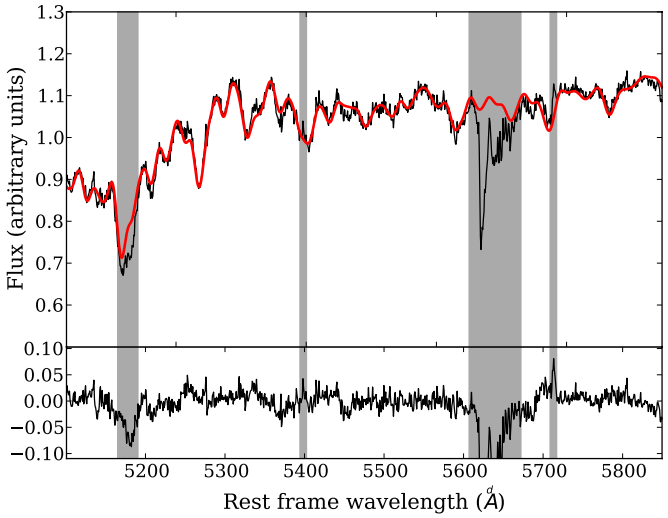

Figure 7. Fit of the velocity dispersion of the lens. Top: the red curve is the best-fit synthetic spectrum. Shaded regions are masked and not used for the fit. Bottom: residuals of the fit in fractions of the total flux.

(A color version of this figure is available in the online journal.)

we fit SPS models to the observed SED of the galaxy. A measurement of this kind was already performed by Grillo et al. (2009) and Auger et al. (2009, hereafter Paper IX) for the same object. Their results agree within the errors. Grillo et al. (2009) used Sloan Digital Sky Survey (SDSS) multiband photometry (u, g, r, i, z bands) as their observed SED. In Paper IX, high-resolution *HST* data were used, but only in two bands (F814W and F606W). Auger et al. (2009) also introduced a powerful statistical analysis method, based on Bayesian statistics that allows for physically meaningful priors on the model parameters as well as a full exploration of uncertainties and correlation between the inferred parameters. With five-band *HST* photometry we can now extend the analysis of Paper IX, to obtain a more robust estimate of the stellar mass.

The fitting method is the same as that developed by Auger et al. (2009), and can be summarized as follows. Composite stellar population models are created from Bruzual & Charlot (2003) stellar templates. The star formation history is modeled with a single exponentially decaying burst. The parameters of the model are age, metallicity, exponential burst timescale, dust reddening, and stellar mass. The parameter space is explored using an MCMC routine, through which the posterior PDF is characterized. The stellar templates used are based on either a Salpeter or a Chabrier IMF. For the description of the photometry of the lens we use the double-tPIEMD model described in Section 2.2, that is consistent with the analyses presented in the following sections. The stellar masses of the two components are fitted independently. Results are listed in Table 8, together with the values previously found by Grillo et al. (2009) and Auger et al. (2009).

Table 8
Stellar Mass of the Foreground Lens, from SPS Models

IMF	Chabrier $\log(M_*/M_\odot)$	Salpeter $\log(M_*/M_\odot)$	
Comp. 1	$10.85^{+0.09}_{-0.06}$	$11.13^{+0.05}_{-0.11}$	This work
Comp. 2	$11.27^{+0.05}_{-0.08}$	$11.52^{+0.06}_{-0.08}$	This work
Total	11.40 ± 0.06	11.66 ± 0.06	This work
	$11.38^{+0.04}_{-0.12}$	$11.61^{+0.02}_{-0.08}$	Grillo et al. (2009)
	11.34 ± 0.12	11.59 ± 0.12	Auger et al. (2009)

The analysis reveals the presence of dust for component 1, coherent with our previous findings. Repeating the fit with the dust-corrected magnitudes yields indistinguishable stellar masses. The logarithm of the stellar masses changes by 0.06 if we use the description of the light profile with Sérsic components instead of tPIEMDs. This is due to the different behavior at large radii of the two profiles. Differences in the mass within the outer Einstein radius for the two models are instead well within the measurement errors.

6. A SINGLE COMPONENT MODEL: MEASURING THE AVERAGE SLOPE

In this section we present a single-component lensing and dynamics study of the foreground galaxy, where the total density distribution of the lens is described with a power law. The goal is to obtain a measurement of the slope of the total mass profile and also to test the accuracy allowed by our data in constraining mass models. The system, with its two Einstein rings, offers more constraints than typical single-source lenses. However, the analysis is complicated by the presence of two different lenses along the line of sight. Light rays from the second source are first deflected by the object corresponding to the inner ring and then by the foreground lens, with the result that, unlike the single lens case, the relation between the size of the outer Einstein ring and the enclosed projected mass of the lens is nontrivial. Nevertheless, this can be properly accounted for as described below.

A first lens modeling of the system was carried out in Paper VI. The procedure adopted there was a conjugate points method: multiply imaged spots in the lensed features are identified, and the lens model is determined by minimizing the distance between the corresponding points in the source plane. This is a conservative approach, since it does not make use of all of the information from the surface brightness of the rings. The main lens was modeled as a power-law ellipsoid, with dimensionless surface mass density $\kappa \equiv \Sigma/\Sigma_{\rm cr}$ given by

$$\kappa(\boldsymbol{r}, z_s) = \frac{b_\infty^{\gamma'-1}}{2}(x^2 + y^2/q^2)^{(1-\gamma')/2}\frac{D_{\rm ls}}{D_{\rm os}}, \qquad (2)$$

where $b_\infty = 4\pi(\sigma_{\rm SIE}/c)^2$ and $D_{\rm ls}$ ($D_{\rm os}$) is the angular diameter distance of the source relative to the lens (observer). The second lens (first source corresponding to the brighter arc) was modeled as a singular isothermal sphere (SIS). The model parameter space was explored via an MCMC. The results showed that two types of solution are possible: a model with larger $\sigma_{\rm SIE}$, shallower slope γ' and less massive second lens, or a model with a more massive second lens and steeper main lens slope (see Figure 9 of Paper VI; or black contours of Figure 8). Part of this degeneracy was due to our ignorance of the redshift of the outer ring.

In this paper we use the lens model of Paper VI described above and improve it by incorporating (1) our measurement of the photo-z of the outer ring and (2) a stellar dynamics analysis.

6.1. Stellar Dynamics Modeling

We wish to use our measurements of the velocity dispersion profile of the lens to constrain our lens models. This is done with a procedure similar to that adopted by Suyu et al. (2010), which can be described as follows. For a given model provided by the lensing analysis, we compute a model velocity dispersion profile and compare it to the observed one. The model velocity dispersion is obtained by solving the spherical Jeans equation:

$$\frac{1}{\rho_*}\frac{d\rho_*\sigma_r^2}{dr} + 2\frac{\sigma_\theta^2}{r} = -\frac{GM(r)}{r^2}, \quad (3)$$

where $\rho_*(r)$ is the density distribution of the light, σ_r and σ_θ are the radial and tangential components of the velocity dispersion tensor, $M(r)$ is the total mass enclosed within the spherical shell of radius r. We impose spherical symmetry in the mass model by adopting a spheroidal mass distribution

$$\rho(r) \propto r^{-\gamma'} \quad (4)$$

with normalization chosen such that the total projected mass enclosed within the Einstein radius equals that of the corresponding circularized lens model. The light distribution is described as the sum of two tPIEMD profiles, with the same parameterization described in Section 2.2 (best-fit parameters are in Table 3). The 3D stellar distribution corresponding to the surface brightness profile (1) used to fit the photometry is

$$\rho(r) = \rho_c r_c^2 \left[\frac{1}{r_c^2 + r^2} - \frac{1}{r_t^2 + r^2}\right], \quad (5)$$

with $r \equiv x^2/q_* + q_* y^2 + z^2$. Here we set the axes ratios q_* to one, as we are assuming spherical symmetry.

We then assume an Osipkov–Merritt model for the velocity dispersion tensor (Osipkov 1979; Merritt 1985):

$$\frac{\sigma_\theta^2}{\sigma_r^2} = 1 - \frac{r^2}{r_a^2 + r^2}, \quad (6)$$

where r_a is the anisotropy radius (orbits are radially anisotropic beyond r_a). Finally, we simulate the line-of-sight velocity dispersion measured in our apertures. Rotation is neglected. Although the lens is seen to be rotating, its mean velocity is small compared to the velocity dispersion and should not contribute much to the dynamics of the object. The effect of this approximation will be discussed further below.

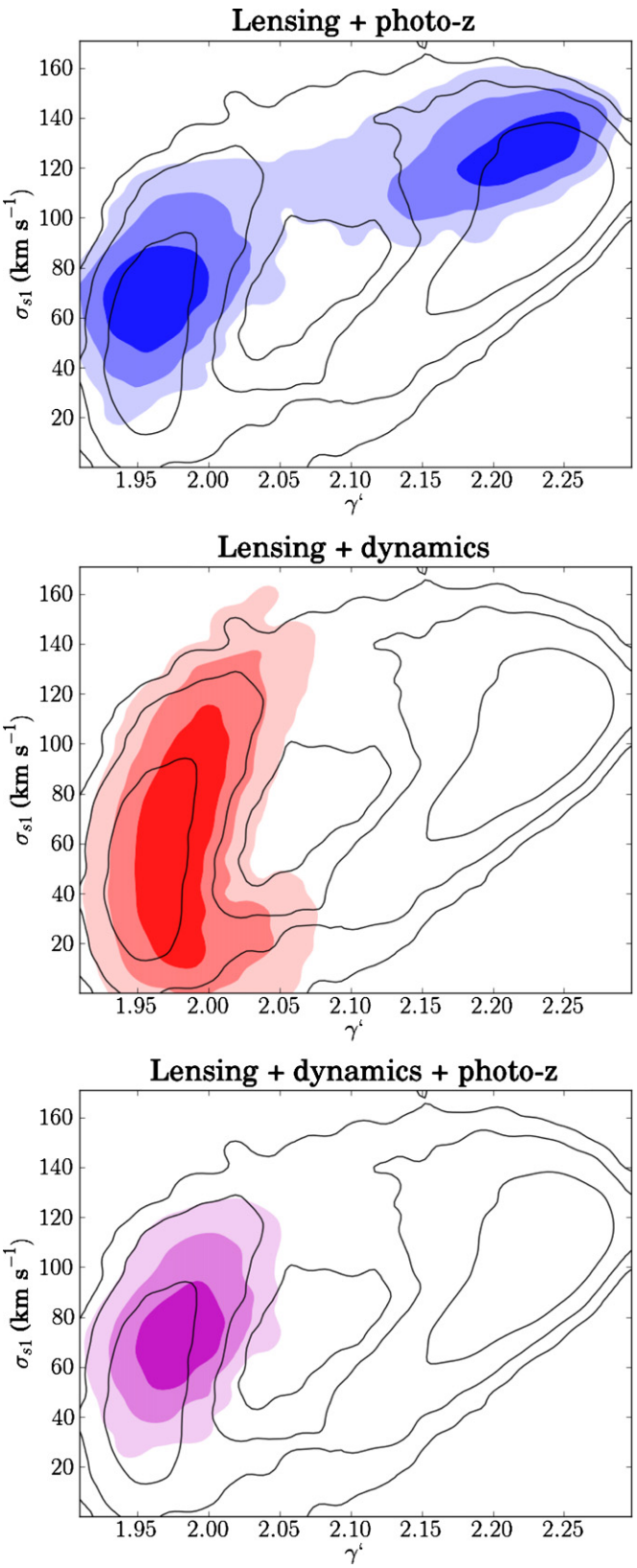

Figure 8. Posterior PDF of γ' and σ_{s1} of the updated (filled contours) lens model, together with the old model of Paper VI (empty contours). The updated model includes only the photo-z measurement of the outer ring in the top panel, only the velocity dispersion profile of the lens in the middle panel, and both the photo-z and velocity dispersion profile in the bottom panel. The levels correspond to 68%, 95%, and 99.7% enclosed probability.

(A color version of this figure is available in the online journal.)

6.2. Combining the Constraints

The models of the lens are defined by the set of parameters $\boldsymbol{\eta} \equiv \{\sigma_{\rm SIE,lens}, \gamma', \sigma_{\rm SIS,s1}, z_{s2}\}$: the strength and power-law index of the foreground lens, the strength of the background lens, and the redshift of the outer ring, respectively. Each model gives a prediction of the velocity dispersion in each aperture, $\sigma_{{\rm ap},i}^{(\rm mod)}$. The new posterior probability distribution for the model is obtained via importance sampling: the MCMC sample corresponding to the lens modeling of Paper VI is weighted by the likelihood of the measurements $\mathbf{d} \equiv \{z_{s2}, \sigma_{{\rm ap},i}^{(\rm meas)}\}$ given the model parameters $\boldsymbol{\eta}$. The following likelihood function is used:

$$L(\mathbf{d}|\boldsymbol{\eta}) = P_z(z_{s2}) \prod_i G_i\left(\sigma_{{\rm ap},i}^{(\rm meas)}|\boldsymbol{\eta}\right), \tag{7}$$

where $P_z(z_{s2})$ is the PDF in Figure 4 and

$$G_i\left(\sigma_{{\rm ap},i}^{(\rm meas)}|\boldsymbol{\eta}\right) = \frac{1}{\sqrt{2\pi\Delta_{\sigma,i}^2}} \exp - \frac{\left(\sigma_{{\rm ap},i}^{(\rm meas)} - \sigma_{{\rm ap},i}^{(\rm mod)}\right)}{2\Delta_{\sigma,i}^2}, \tag{8}$$

and $\sigma_{{\rm ap},i}$ and $\Delta_{\sigma,i}$ are the zeroth and second moment of the posterior PDF of the measured velocity dispersion in aperture i, respectively.

In Figure 8 we show the updated posterior PDF obtained by importance sampling with the photo-z and dynamics measurements, both separately and jointly. It is clear that although photo-z and stellar kinematics alone leave some degeneracies, the posterior PDFs are almost perpendicular in this space, and therefore the combination of the two is particularly effective. The estimate of the slope obtained by marginalizing over the other parameters is

$$\gamma' = 1.98 \pm 0.02. \tag{9}$$

We stress that our uncertainty on this parameter is a factor of four smaller than the typical error on γ' from studies of single-source gravitational lenses with SDSS spectroscopy (Auger et al. 2010a; see Figure 15). Comparable precision was reached by Barnabè et al. (2011) for a sample of lens systems with two-dimensional kinematics constraints from integral field spectroscopy.

In order to better understand the significance of these results, we try to quantify the error introduced by our simplified model for the stellar dynamics. Two of our assumptions are potential sources of bias: spherical symmetry and the non-rotating approximation. The uncertainty in the mass determination from kinematics data is of the order of $\delta\sigma^2/\sigma^2 \sim 10\%$. Biases on the order of this uncertainty or smaller are unlikely to bring significant changes to the results of our analysis. By considering only the velocity dispersion and neglecting rotation, we underestimate the mass of the galaxy by a factor $\sim(v_{\rm rot}/\sigma)^2$, which is within 10% in all apertures but one. To gauge the importance of this effect we perform the following test. We fit the model velocity dispersion profiles to the following "effective velocity dispersion": $\sigma_{\rm eff} \equiv \sqrt{\sigma^2 + v_{\rm rot}^2}$. We then apply the same importance sampling procedure described above to get a new constraint on the density slope γ'. The new estimate with 1σ uncertainty is

$$\gamma' = 1.97 \pm 0.02, \tag{10}$$

which is consistent with the original estimate given by Equation (9). On the basis of this result, we can conclude that our approximation of non-rotating halo introduces a systematic error of the order of 0.01 on the inferred value of the slope γ'.

Quantifying the systematics introduced by the spherical symmetry assumption is more complicated. In a previous work, Barnabè et al. (2011) performed a robust dynamical modeling of 12 SLACS lenses previously analyzed with a spherical Jeans equation approach by Auger et al. (2010a). The slopes γ' inferred by Auger et al. (2010a) are consistent with the more accurate measurements of Barnabè et al. (2011), with a bias on γ' of 0.05 ± 0.04. However, the uncertainty on γ' that we achieve in our work is smaller than that and an estimate of the bias requires additional work. Two distinct effects come into play. First, the lens has a non-circular projected shape in both its mass and light distribution. Second, the galaxy may even have asymmetries along the line of sight. The importance of these effects on our analysis is quantified in Appendix B. By relaxing the assumption of spherical symmetry the additional uncertainty on the velocity dispersion is about $\delta\sigma^2/\sigma^2 \sim 10\%$. It follows that none of our results change appreciably.

An independent analysis of the system was carried out by Vegetti et al. (2010). The method adopted by them is more complex than the one used in Paper VI: they made use of information from all the pixels of the lensed features to reconstruct the source surface brightness as a whole. Using data from the inner ring only, they obtained the following estimate for the density slope:

$$\gamma' = 2.20 \pm 0.03^{(\rm stat)}. \tag{11}$$

This is a local estimate of the slope γ', obtained by measuring the magnification of the arc in the radial direction. Our measurement is instead an average slope, obtained by fitting a single power-law halo to data spanning the lens from the center (dynamics) to the outer lensed ring. This difference may suggest that the actual mass distribution of the lens is different from a simple power-law halo. It is also for this reason that we proceeded to model the system with a more complex model.

7. A TWO-COMPONENT ANALYSIS: DISSECTING LUMINOUS AND DARK MATTER

We perform a two-component lensing and dynamics study where the mass distribution is composed of a DM halo and a bulge of stars.

7.1. Lensing and Dynamics Modeling

We use a power-law ellipsoid for the DM, while the stars are described with the double-tPIEMD model found from the photometry analysis. The second lens is again modeled as an SIS. The parameters of the stellar distribution are fixed to the best-fit values reported in Table 3. The global mass-to-light ratio is left as a free parameter, but the relative contribution of the two components is fixed according to the results of the SPS analysis presented in Section 5. For a unit F814W-band magnitude, component 1 is measured to be a factor of 1.73 (1.77) heavier than component 2 assuming a Salpeter (Chabrier) IMF. In our lensing model, the mass-to-light ratio of component 1 is set to be 1.75 times larger than for component 2.

We also allow for constant external shear $\gamma_{\rm ext}$ with position angle P.A.$_{\rm ext}$ and constant external convergence $\kappa_{\rm ext}$ in the lens plane. Issues related to the external convergence are discussed below in a dedicated subsection. Compared to the lensing study presented in the previous section, this model has two additional free parameters: the stellar mass $M_*^{\rm LD}$ and the external

convergence $\kappa_{\rm ext}$. Given the very tight constraint on the average slope γ' from the single component analysis, we expect to be able to determine both the slope of the DM halo $\gamma_{\rm DM}$ and the stellar mass $M_*^{\rm LD}$ with sufficient accuracy. The range of values of the slope of the DM halo explored in this analysis is $1.0 < \gamma_{\rm DM} < 3.0$.

The technique adopted to fit the model to the lensing data is the same used for Paper VI: a conjugate points method implemented with an MCMC. The dynamics analysis is carried out with a procedure very similar to the one described in Section 6.1: we solve the spherical Jeans equation for our model and obtain a synthetic velocity dispersion profile to be compared to the measured one. The (spherically symmetric) model mass distribution is obtained by circularizing the projected mass distribution of the lens model, setting $q_{\rm DM}$ and q_* to one, and by taking the corresponding spherical deprojections. The light distribution is set by circularizing the double-tPIEMD profile specified in Table 3.

We then proceed to incorporate information on stellar dynamics and on the redshift of the background source. This is done by importance sampling, with the same method described in Section 6.2.

7.2. External Convergence

Objects other than the main lens can contribute to the surface mass density κ. This external convergence is hard to detect and is degenerate with the total mass of the lens galaxy. Ignoring the contribution to κ from perturbers can lead in principle to a bias in the measurement of the key parameters of the lens. In order to take into account the effect of external convergence on our error budget, we include it in our model by generating random values of $\kappa_{\rm ext}$ drawn from a plausible distribution. This procedure allows us to propagate correctly this uncertainty to the other model parameters. Kinematics information can also help to constrain $\kappa_{\rm ext}$ to some extent, as it is only sensitive to the mass dynamically associated with the galaxy, in contrast to lensing that is sensitive to all mass structures along the line of sight to the source.

Insight on the actual value of $\kappa_{\rm ext}$ can be gained by studying the lens environment. According to Treu et al. (2009), this is found to be marginally underdense with respect to average lines of sight, therefore there is no evidence for the presence of a group in the lens neighborhood. The closest cluster known to the NASA/IPAC Extragalactic Database (NED) is MaxBCGJ146.87912+10.07800, at redshift $z = 0.151$ and projected distance 8.70 arcmin from our lens (Treu et al. 2009). If we assume an SIS profile for the cluster with a typical value for its velocity dispersion $\sigma = 1000\,{\rm km\,s^{-1}}$ we obtain a contribution to the convergence $\kappa_{\rm cl} < 0.01$. We also scanned the SDSS archive looking for massive red galaxies within $5'$ of the lens. Only one ETG was found, at a redshift $z = 0.218$ and angular distance $2'.6$. If we assume that this object is the brightest galaxy of a group and associate it with an SIS halo of $\sigma = 500\,{\rm km\,s^{-1}}$ the corresponding convergence at the location of the lens is $\kappa = 0.02$. Finally, the lensing analysis of Gavazzi et al. (2008) quantified the external shear as $\gamma_{\rm ext} = 0.07$ directed -31° east of north. The *HST* images show two objects with the same alignment relative to the lens (see Figure 3). If we make the assumption that those objects are responsible for the shear and assume again an SIS profile we obtain $\kappa_{\rm ext} = |\gamma_{\rm ext}| = 0.07$.

Hilbert et al. (2007) studied the external convergence associated with strong lensing systems in cosmological simulations. They found that for a source at redshift $z_s = 5.7$ the distribution of $\kappa_{\rm ext}$ is skewed with a peak at -0.04, has zero mean and a scatter of 0.05. A slightly smaller scatter and a peak at -0.02 is found by Suyu et al. (2010) for sources at $z_s = 1.39$.

Taking all these aspects into account, we adopt as prior for $\kappa_{\rm ext}$ in our analysis a Gaussian distribution peaked at 0.05, with dispersion $\sigma_\kappa = 0.05$ and truncated to values in the interval $-0.05 < \kappa_{\rm ext} < 0.15$. This range should capture the indication of a positive contribution from the object responsible for the shear and take into account the effect of random mass clumps along the line of sight. Priors with a broader range of allowed values of $\kappa_{\rm ext}$ lead to larger uncertainties on the other model parameters, but none of the conclusions of our study are altered.

7.3. Results

Contour plots of the posterior PDF for the model parameters are shown in Figures 9 and 10. The inference on the two key parameters M_* and $\gamma_{\rm DM}$ is shown in better detail in Figure 11. The best-fit velocity dispersion profile is plotted in Figure 12. By marginalizing over the remaining parameters, our model constrains the stellar mass to

$$M_* = 5.5^{+0.4}_{-1.3} \times 10^{11}\,M_\odot. \quad (12)$$

This estimate comes from lensing and dynamics data, and does not rely on assumptions on the mass-to-light ratio of the stars. This value will be compared with the measurement of the stellar mass obtained independently from photometry.

Another important result is the constraint that we obtain on the slope of the DM halo:

$$\gamma_{\rm DM} = 1.7 \pm 0.2. \quad (13)$$

This result shows strong evidence for a contraction of the DM distribution relative to the r^{-1} inner slopes typical of DM-only simulations (Navarro et al. 1997). Figure 13 shows the mean density profile of each mass component compared to the mean single power-law fit from Section 6.

Our inference for the anisotropy radius constrains $r_a > 13$ kpc, meaning that radial anisotropy is ruled out in the region probed by our data. This is consistent with previous work (e.g., Koopmans & Treu 2003; Treu & Koopmans 2004) and expected on theoretical grounds because strong radial anisotropy would lead to instabilities.

In contrast to the power-law model considered in the previous section, this mass model has a density distribution with a slope that changes with radius. It is interesting to compare the local value of the slope at the location of the inner ring with the measurement of Vegetti et al. (2010). Vegetti et al. (2010) modeled the *HST* F814W image using only lensing information from the inner ring. Lensing is only sensitive to projected masses, therefore, in order for the comparison to be meaningful, we have to consider the logarithmic slope of the total projected mass distribution, evaluated at the inner Einstein radius. We find

$$\frac{d\log\kappa}{d\log r} = -1.1 \pm 0.1. \quad (14)$$

This value is consistent with the slope found by Vegetti et al. (2010), which is given by $-(\gamma' - 1) = -1.2$, where γ' is the slope of the 3D mass distribution given in Equation (11).

Finally, it is interesting to note how the inference on the stellar mass is rather insensitive to the actual value of the redshift of the second source, z_{s2} (see Figure 9). This means that, with the current data quality, a spectroscopic measurement of the redshift of the outer ring would not bring significantly more information.

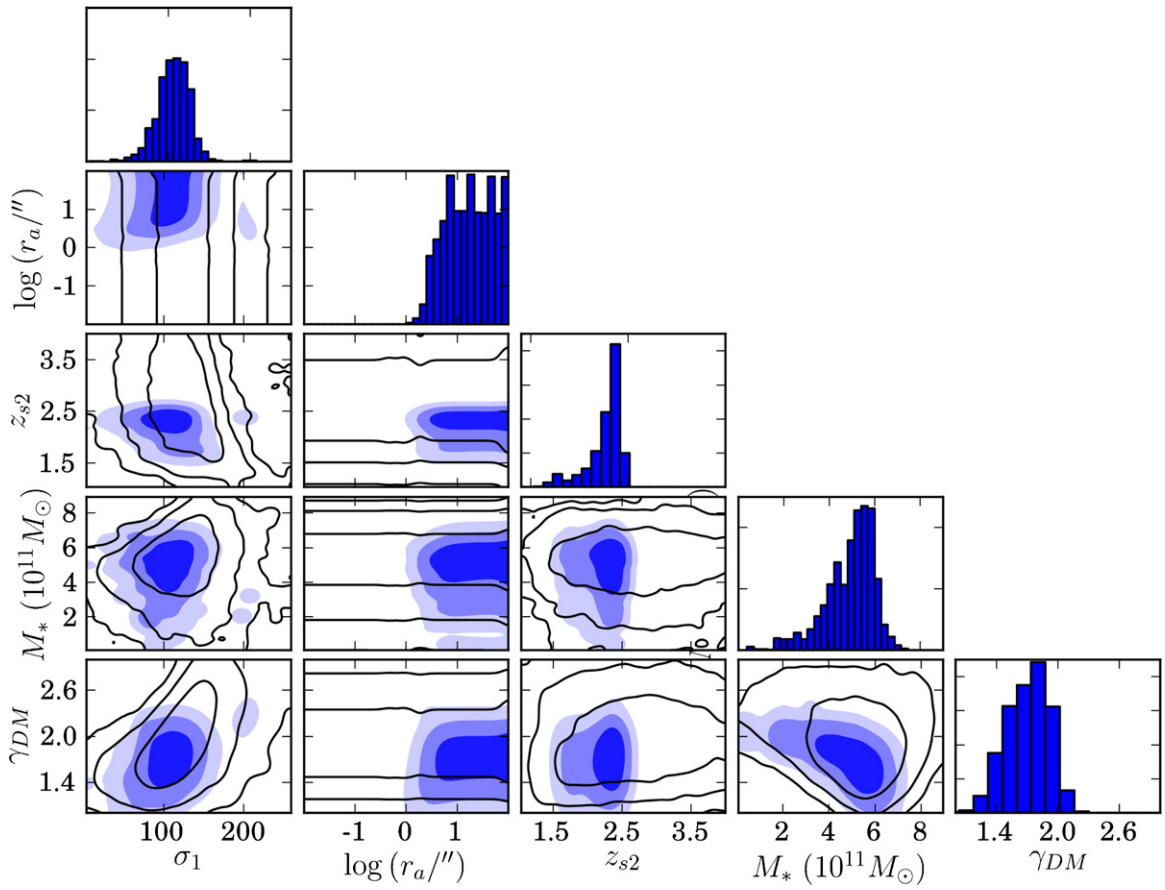

Figure 9. Posterior PDF in the multidimensional space spanned by the stellar mass $M_*^{\rm LD}$, slope of the dark matter halo $\gamma_{\rm DM}$, radial anisotropy scale radius r_a, strength of the second lens σ_{s1}, and redshift of the second source z_{s2}. The levels correspond to 68%, 95%, and 99.7% enclosed probability. Solid contours: constraints from lensing only. Shaded regions: constraints from lensing, dynamics, and photo-z.

(A color version of this figure is available in the online journal.)

8. DISCUSSION

8.1. Luminous and Dark Matter in the Lens

The data in our possession allowed us to study the lens galaxy of the system SDSSJ0946+1006 under multiple aspects. Thanks to the high-resolution photometry from *HST* we were able to note now the light distribution is well described with two components, while single-component models yield poor fits. These two components appear to be nearly perpendicular (in projection), have significantly different effective radii and surface brightnesses. The colors of the more compact component (component 1 from now on) are also significantly redder (see Table 4), indicative of an older or more metal-rich stellar population. As we will discuss below, these characteristics suggest a particular scenario for the past evolution of this object.

In Sections 5 and 7, we presented two independent measurements of the stellar mass of the foreground galaxy of the system SDSSJ0946+1006 derived with a lensing+dynamics analysis and with an SPS study. The measured values of M_*, obtained by marginalizing over the other model parameters, are reported in Table 9.

The stellar mass measured from gravitational lensing and dynamics, $M_*^{\rm LD}$, is larger than the masses obtained from the SPS study, $M_*^{\rm SPS}$. This discrepancy can be quantified with the "IMF mismatch" parameter $\alpha \equiv M_*^{\rm LD}/M_*^{\rm SPS}$, also reported in Table 9. A Salpeter IMF is clearly favored, while the probability of the IMF being heavier than Chabrier ($\alpha_{\rm Chab} > 1$) is 95%.

Table 9
Stellar Mass of the Foreground Galaxy

Method	M_* $(M_\odot)$	α[a]
Lensing+dynamics	$5.5^{+0.4}_{-1.3} \times 10^{11}$	
SPS, Chabrier IMF	$(2.5 \pm 0.3) \times 10^{11}$	2.0 ± 0.4
SPS, Salpeter IMF	$(4.5 \pm 0.6) \times 10^{11}$	1.1 ± 0.2

Note. [a] α is the IMF mismatch parameter defined as $\alpha \equiv M_*^{\rm LD}/M_*^{\rm SPS}$.

This result is in agreement with a general trend observed by Grillo et al. (2009), Treu et al. (2010), and Auger et al. (2010b) for the ETGs of the SLACS sample. They find that, on average, a Salpeter IMF better matches the measurements of stellar masses from lensing and dynamics. A similar result is found by Spiniello et al. (2011) for a very massive ETG. As discussed extensively by Treu et al. (2010), stellar mass and slope of the DM halo are degenerate with respect to typical lensing and dynamics constraints: given a bulge-halo decomposition, steepening the DM profile and decreasing the stellar mass can result in fits to the observed velocity dispersion and mass within the Einstein radius as good as the original model. Treu et al. (2010) explained how the observed trend of increasing α with velocity dispersion can either be interpreted as the effect of a correlation between IMF or DM inner slope with total mass. Auger et al. (2010b) explored this degeneracy by considering adiabatically contracted DM halos set by an imposed relation between stellar and virial mass, and found preference for a stellar mass-to-light ratio closer to

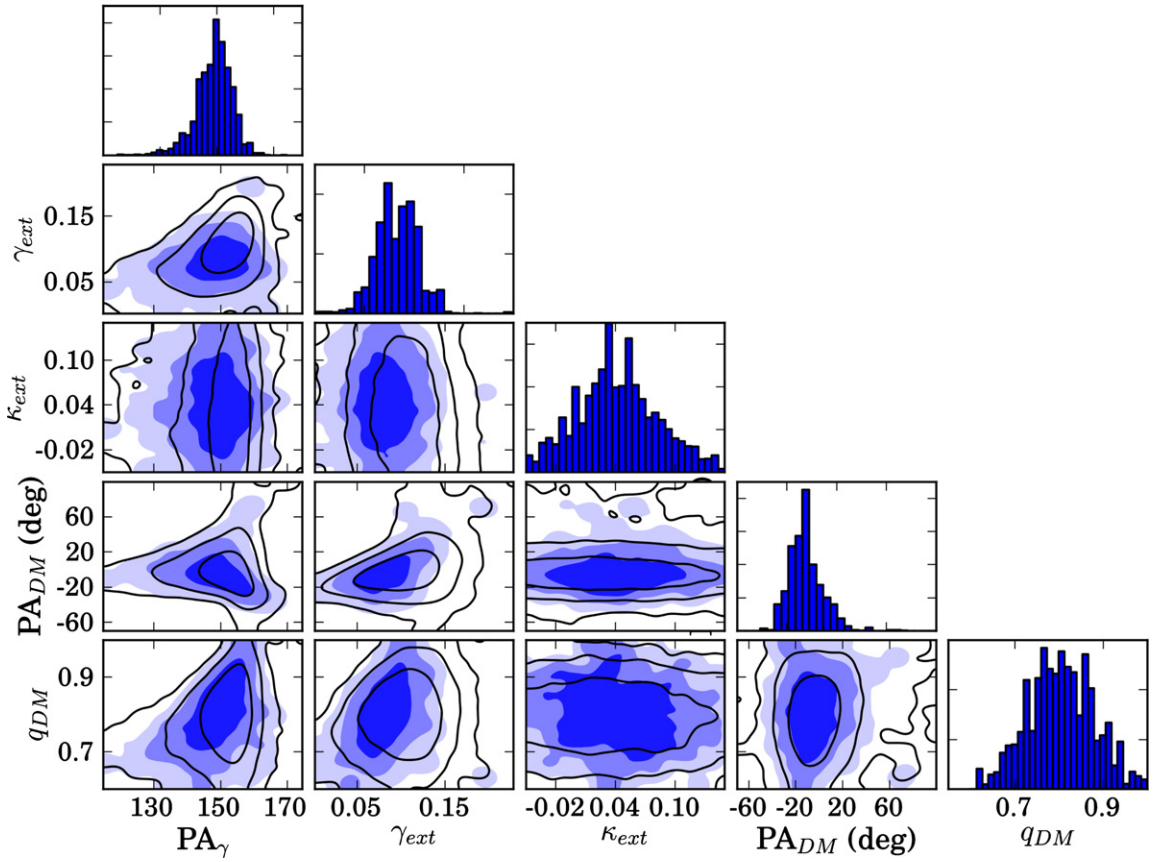

Figure 10. Posterior PDF in the multidimensional space spanned by external convergence $\kappa_{\rm ext}$, strength and position angle of the external shear, $\gamma_{\rm ext}$, P.A.$_{\rm ext}$, axis ratio of the dark matter halo $q_{\rm DM}$, position angle of the major axis of the dark matter halo, P.A.$_{\rm DM}$. The levels correspond to 68%, 95%, and 99.7% enclosed probability. Solid contours: constraints from lensing only. Shaded regions: constraints from lensing, dynamics, and photo-z.

(A color version of this figure is available in the online journal.)

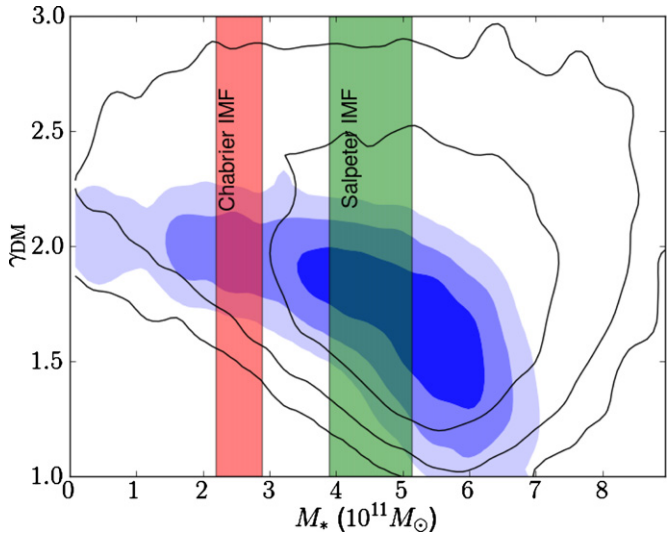

Figure 11. Posterior PDF projected in the space $M_* - \gamma_{\rm DM}$. The vertical shaded regions show independent measurements of the stellar mass from photometry, presented in Section 5.

(A color version of this figure is available in the online journal.)

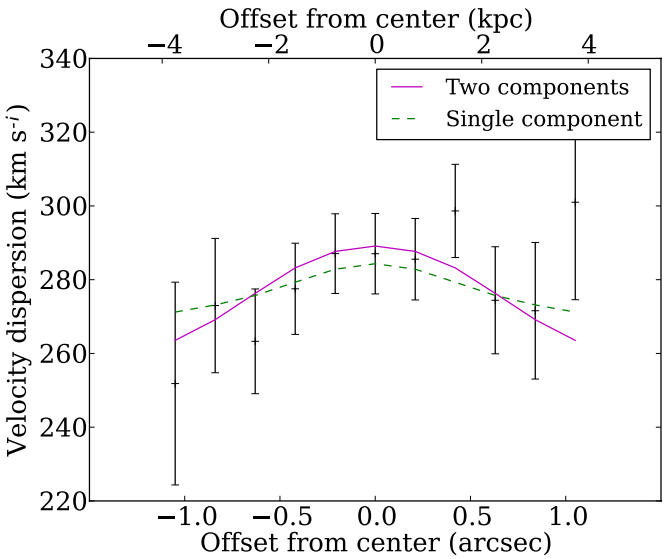

Figure 12. Best-fit velocity dispersion profile of the lens. Solid line: two components model. Dashed line: single power-law model.

(A color version of this figure is available in the online journal.)

a Salpeter than a Chabrier IMF. Similarly, Napolitano et al. (2010) find that a Kroupa IMF, which has a mass-to-light ratio slightly larger than a Chabrier IMF, fits adiabatically contracted DM halos well. In the present study we allowed the slope of the DM halo of our lens galaxy to vary freely. Its measured value, $\gamma_{\rm DM} = 1.7^{+0.2}_{-0.2}$, is significantly steeper than the inner slope of a Navarro–Frenk–White (NFW) halo. Still, we find a stellar mass larger than what can be accounted for with a Salpeter IMF and not compatible with a Chabrier IMF. Our results imply that a Salpeter IMF provides a far better description of the mass-to-

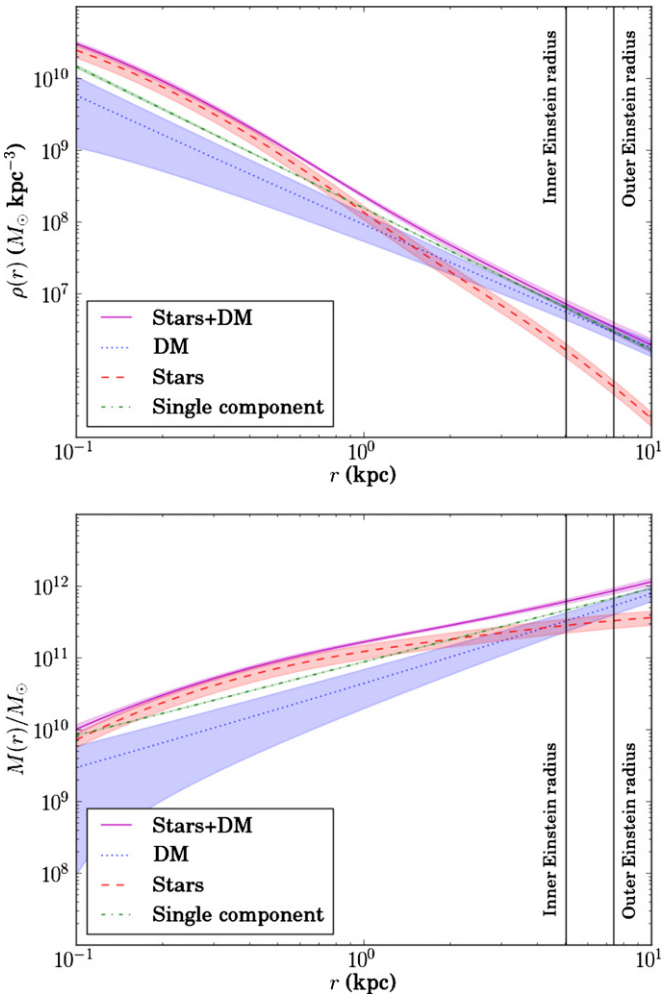

Figure 13. Best-fit density (top) and mass (bottom) profiles. Solid line: total mass from bulge-halo decomposition. Dashed line: stellar mass. Dotted line: dark matter. Dash-dotted line: total mass from single-component analysis. The shaded regions represent 1σ uncertainties.

(A color version of this figure is available in the online journal.)

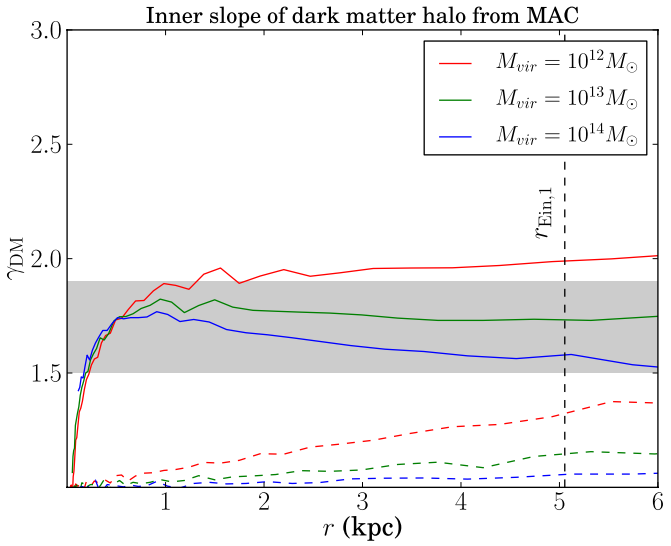

Figure 14. Solid lines: inner slope of the dark matter halo for modified adiabatic contraction (MAC; Gnedin et al. 2004) models. Dashed lines: slope of the non-contracted (NFW) dark matter halo. Shaded region: 68% confidence interval of the slope measured in this paper.

(A color version of this figure is available in the online journal.)

light ratio of the stellar population than a Chabrier IMF even with a steepened DM halo. This result is consistent with the recent findings of Cappellari et al. (2012) and van Dokkum & Conroy (2011).

In contrast, Salpeter-like IMFs are typically ruled out for lower mass systems (Cappellari et al. 2006; Ferreras et al. 2010) or spiral galaxies (Bell & de Jong 2001; Dutton et al. 2011; Suyu et al. 2012; Brewer et al. 2012).

The lensing and dynamics analysis presented in Section 7 showed evidence for contraction of the DM halo with respect to a baryonless NFW profile. A similar result is found by Grillo (2012) for an ensemble measurement of 39 massive elliptical galaxy lenses. This result is in qualitative agreement with many theoretical studies of the evolution of spheroidal galaxies (Blumenthal et al. 1986; Gnedin et al. 2004; Gustafsson et al. 2006; Abadi et al. 2010; Duffy et al. 2010). Duffy et al. (2010) in their simulations of redshift $z = 2$ galaxies find inner DM slopes that span the range $1.4 < \gamma_{\rm DM} < 2.0$ depending on the different prescriptions adopted to model the effect of the baryons. Our measured value of $\gamma_{\rm DM}$ falls nicely in that range, although our galaxy is at significantly lower redshift. Gnedin et al. (2004) provide a prescription to calculate the DM profile of their modified adiabatic contraction (MAC) model. It is interesting to test the MAC model on the measured slope of the DM halo of our galaxy. The final DM density profile of the MAC model of Gnedin et al. (2004) is determined given the observed light profile, the concentration parameter c of the original (non-contracted) NFW halo and the baryon mass fraction within its virial radius, f_b.

Since we do not have information on the initial properties of the DM halo of our galaxy, we use a few trial values of the virial mass $M_{\rm vir}$, spanning a plausible range indicated by a weak lensing study of ellipticals (Gavazzi et al. 2007), and employ a mass–concentration relation from Macciò et al. (2008) based on *WMAP5* cosmological parameters. We then calculate the inner slope of the final DM distribution with the software Contra (Gnedin et al. 2004). The inferred inner slope for $\log(M_{\rm vir}/M_\odot) = 12.0, 13.0, 14.0$ is plotted in Figure 14. Despite the large range of virial mass explored, the slopes of the contracted halos lie around $1.5 < \gamma_{\rm DM} < 2.0$ over the spatial region covered by our data. The MAC model is therefore able to reproduce our measurement of the DM halo slope.

8.2. A Formation Scenario

As our data show, the stellar distribution in the lens galaxy consists of two components that differ in alignment, surface brightness and stellar population. This particular structure suggests different formation histories for the two components. The bright and compact component may have formed first, and later on accreted stellar systems in the outskirts without disrupting the structure of the original bulge. Alternatively, component 2 might have been present originally and component 1 be formed in a star formation event following a wet merger. We point out that in the infrared image we see evidence for tidal distortion in the outskirts of the galaxy (see Figure 3), possible indication of an ongoing merger. Part of the faint extended envelope of component 2 could be material accreted relatively recently. The presence of the dust lane in the center of the galaxy (see Appendix A) may also be the result of a recent merger. We also note that Vegetti et al. (2010) detected a compact substructure

of mass $\sim 3 \times 10^9\ M_\odot$ located in the proximity of the inner ring image, indicating that minor mergers may still be occurring.

Let us consider our first hypothesis: the galaxy consisted initially of the compact component 1. What are the structural parameters of component 1 and how does it relate to other elliptical galaxies? Its effective radius is $r_{\rm eff} = 0\farcs50$ (see Tables 2 and 3), which corresponds to a physical radius of 1.79 kpc. Similar effective radii are found for high-redshift ($z > 1.2$) ellipticals (Daddi et al. 2005; Trujillo et al. 2006; van Dokkum et al. 2008). Its stellar mass as inferred from the SPS analysis is given by $\log(M_*^{\rm SPS}/M_\odot) = 10.85$ ($\log(M_*^{\rm SPS}/M_\odot) = 11.13$) for a Chabrier (Salpeter) IMF. Local ellipticals with similar values of the stellar mass have effective radii a factor of a few larger than this object (Shen et al. 2003; Hyde & Bernardi 2009). Analogously, the high-redshift objects of Daddi et al. (2005), Trujillo et al. (2006), and van Dokkum et al. (2008) are also significantly more massive than local galaxies with similar effective radii. Finding objects in the local universe that correspond to these high-redshift "red nuggets" is in fact a standing problem in the study of elliptical galaxies. It is not clear how objects initially so compact evolve into the more diffuse galaxies that we observe at recent times.

Recent numerical simulations (Hopkins et al. 2009a; Oser et al. 2012) showed how minor dry mergers can increase the size of elliptical galaxies significantly, with the stars of the accreted objects that grow the outskirts of the galaxy, even though the observed and predicted merger rates are such that this mechanism might not be sufficient (Newman et al. 2012). The observational signature of this process would be the presence of a compact core, the original red nugget, surrounded by a more diffuse distribution of stars from the accreted systems. The galaxy studied in this paper might be one of these objects.

9. SUMMARY

We have presented a new set of photometric and spectroscopic data for the gravitational lens system SDSSJ0946+1006. We used these data to constrain the structural properties of the foreground elliptical galaxy of the system. On the basis of our results, the following statements can be made.

1. The redshift of the source corresponding to the outer ring is $z_{s2} = 2.41^{+0.04}_{-0.21}$ at 68% confidence level, as revealed by our photo-z measurement.
2. If we describe the total mass distribution with a power-law ellipsoid $\rho \propto r^{-\gamma'}$, lensing and dynamics data give as measured value $\gamma' = 1.98 \pm 0.02 \pm 0.01$. This parameter should be interpreted as an effective slope of the density profile averaged over the region within the outer Einstein ring. The special lensing configuration and the exquisite quality of our data allowed us to measure γ' with unprecedented precision. The value obtained is consistent with isothermal ($\gamma' = 2$) and is in agreement with the general trend observed for the massive ETGs of the SLACS sample, $\langle\gamma'\rangle = 2.078 \pm 0.027$ with intrinsic scatter $\sigma_{\gamma'} = 0.16 \pm 0.02$ (Auger et al. 2010a; Koopmans et al. 2009; Barnabè et al. 2011). See Figure 15 for a comparison of our measurement of γ' with measurements of the same parameter for the SLACS sample of ETGs by Auger et al. (2010a).
3. We are able to decompose dark and stellar matter with lensing and dynamics data, assuming a power-law density profile for the DM. The derived stellar mass is $5.5^{+0.4}_{-1.3} \times 10^{11}\ M_\odot$, consistent with a Salpeter IMF and inconsistent with a Chabrier IMF. This constraint on the IMF is plotted in Figure 15 together with similar measurements for the other SLACS lenses obtained by Treu et al. (2010). Note that we achieve better precision despite using less strict assumptions on the DM profile.
4. The slope of the DM halo is found to be $\gamma_{\rm DM} = 1.7 \pm 0.2$. This is strong evidence for contraction relative to the r^{-1} behavior of NFW profile observed in simulations without baryons, and is in agreement with the inner DM profiles obtained by Duffy et al. (2010) in their simulations of $z = 2$ galaxies and with the MAC model of Gnedin et al. (2004). Our inferred bulge-halo decomposition has a local projected slope at the inner ring in agreement with the value measured by Vegetti et al. (2010) based on a completely independent technique.
5. The particular structure of the stellar distribution, with a compact core and a misaligned faint extended envelope, might be the result of accretion of low-mass systems by a compact red nugget.
6. A spectroscopic detection of the redshift of the outer ring would still help improve the model, but would not lead to a dramatic change in the results of our analysis.

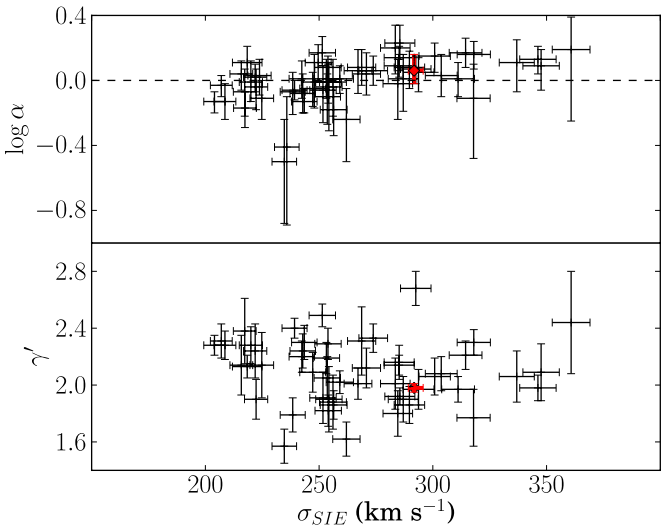

Figure 15. Top panel: IMF mismatch parameter $\alpha \equiv M_*^{\rm LD}/M_*^{\rm SPS}$ relative to a Salpeter IMF vs. lens strength $\sigma_{\rm SIE}$ for the SLACS lenses of Treu et al. (2010) (black crosses) and for the Jackpot (red cross). Measurements of Treu et al. (2010) are obtained assuming an NFW dark matter halo with fixed scale radius for the lensing and dynamics analysis. Bottom panel: average slope of the total density profile γ' vs. lens strength $\sigma_{\rm SIE}$ for the SLACS lenses of Auger et al. (2010a; black crosses) and for the Jackpot (red cross).

(A color version of this figure is available in the online journal.)

Based on observations made with the NASA/ESA *Hubble Space Telescope*, obtained at the Space Telescope Science Institute, which is operated by the Association of Universities for Research in Astronomy, Inc., under NASA contract NAS 5-26555. These observations are associated with programs 11701, 11202, and 10886. Support for those programs was provided by NASA through a grant from the Space Telescope Science Institute, which is operated by the Association of Universities for Research in Astronomy, Inc., under NASA contract NAS 5-26555.

Some of the data presented herein were obtained at the W. M. Keck Observatory, which is operated as a scientific partnership among the California Institute of Technology, the University of California, and the National Aeronautics and

Figure 16. Dust correction. Left panel: dust map of the central part of the galaxy based on F438W, F606W, and F814W images. Dark pixels represent higher column densities of dust. Middle panel: original image in the F336W band. Right panel: dust-corrected F336W band image, showing a single clump of light. The central parts have lower signal-to-noise ratio as a result of the noisy dust map.

Space Administration. The Observatory was made possible by the generous financial support of the W. M. Keck Foundation. The authors wish to recognize and acknowledge the very significant cultural role and reverence that the summit of Mauna Kea has always had within the indigenous Hawaiian community. We are most fortunate to have the opportunity to conduct observations from this mountain.

T. Treu acknowledges support from the Packard Foundation through a Packard Research Fellowship. R. Gavazzi acknowledges support from the Centre National des Etudes Spatiales. P. J. Marshall was given support by the Royal Society in the form of a research fellowship.

APPENDIX A

DUST CORRECTION

The presence of dust complicates our analysis. Nevertheless, we deal with it by applying a procedure similar to that adopted by Koopmans et al. (2003) and Suyu et al. (2009) for the system B1608+656. The details of the procedure are the following.

We select a small region in the center of the galaxy for which we want to apply a dust correction. We estimate the intrinsic colors of this central part by measuring them in a region that we think is free of dust.

We assume a dust law from Cardelli et al. (1989), with $R_V = 3.1$. Given the flux in one band and the colors of the object, the fluxes in the remaining bands are determined by the dust law. Therefore, with images in two or more bands we can constrain both the intrinsic flux and the dust content of the object. In our case we determine these two quantities in the central region of the lens on a pixel-by-pixel basis by fitting the F814W, F606W, and F438W fluxes. We want to check if we can account for the dark lane observed in the F336W image independently from the data in that band, and therefore we do not include that image in our dust analysis. The F160W image is excluded because of its lower spatial resolution. The PSF of the different images is not matched. Our inference on the presence of dust is not affected by this approximation.

The two dust-free colors, F606W–F814W and F438–F606W, are measured in an annulus around the center and inside of the inner ring. We cannot rule out the presence of a uniform dust screen, but that would not affect our conclusions as the tools that we use for quantitative analyses can account for that. The dust-corrected flux in the lens center is then calculated with the fitting method described in Section 5.4 of Suyu et al. (2009). Figure 16 shows the recovered dust map, the F336W image corrected for dust and its original version. It can be clearly seen how the dust map, obtained without using data from the F336W, has largest column density right where we observe the dark lane in the image. In the dust-corrected image, the lens looks indeed more like a single object.

The overall amount of dust is relatively small, as the correction to the total magnitude in the F606W band is approximately 0.10 mag.

APPENDIX B

ELLIPTICITY EFFECTS

The mass and light distributions of the lens galaxy are well approximated by ellipses, but we make the assumption of spherical symmetry for the analysis of the kinematics data. How does this assumption affect the results we present? To answer this question we make use of the axisymmetric version of the Jeans equations (Binney & Tremaine 2008),

$$\bar{v_R^2}(R,z) = \bar{v_z^2}(R,z) = \frac{1}{\rho_*(R,z)} \int_z^\infty dz' \rho_*(R,z') \frac{\partial \Phi}{\partial z'} \quad \text{(B1)}$$

$$\bar{v_\phi^2}(R,z) = \bar{v_R^2} + \frac{R}{\rho_*} \frac{\partial(\rho_* \bar{v_R^2})}{\partial R} + R \frac{\partial \Phi}{\partial R}, \quad \text{(B2)}$$

obtained assuming a distribution of stars of the form $f(E, L_z)$.

We take our best-fit single-component model from Section 6.1 and make it elliptical by assuming that the rotation axis L_z is in the plane of the sky and fixing the projected ellipticities in light and mass to $q_* = 0.95$ and $q = 0.87$, respectively. The first value is the ellipticity of the best single-component fit to the light profile, the latter value is given in Gavazzi et al. (2008). Then we assume isotropy in the velocity dispersion tensor, calculate the line-of-sight velocity dispersion profile in the two possible cases of oblate or prolate ellipsoid, and compare it to the corresponding spherical case. Results are shown in Figure 17. Deviations from spherical symmetry bring differences on the order of a few km s^{-1} on the velocity dispersion profile, well within our uncertainties on the measurements, and therefore are not a concern for possible biases.

More important are the effects of asymmetries along the line of sight. We do not have any direct measurement of the line-of-sight structure of the lens, but from the observed projected flattening we can get information on the intrinsic shape of the galaxy by statistical means. Padilla & Strauss (2008) measured the distribution of intrinsic axis ratios of massive elliptical galaxies. By drawing samples of galaxy shapes from their inferred distribution and assuming random orientations we find that 68% of the objects that produce a projected ellipticity $q_* = 0.95$ have an axis ratio rounder than 0.8. How does the velocity dispersion profile of an oblate (prolate) galaxy with minor (major) axis along the line of sight and axis ratio of 0.8 differ from that of a spherical galaxy with the same

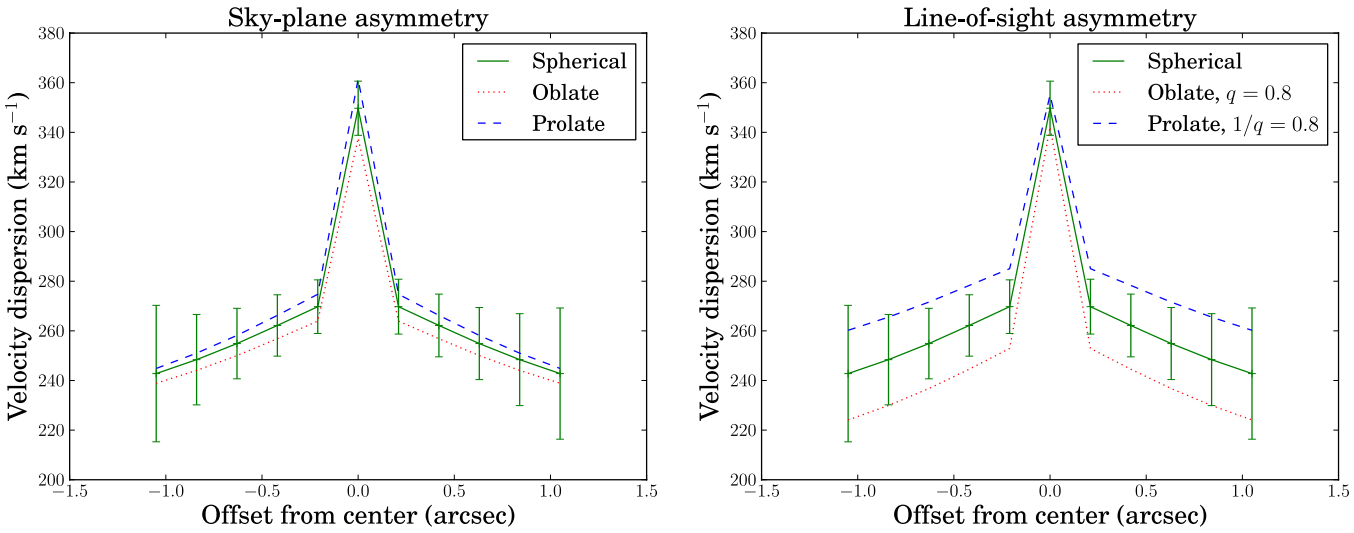

Figure 17. Top: line-of-sight velocity dispersion profile for a spherical model and for elliptical models with $q_* = 0.95$ and $q = 0.87$, calculated by solving the axisymmetric Jeans equation. The models have the same projected mass within the inner Einstein radius. PSF smearing is not included, resulting in the high central peak. Overplotted are the error bars on the measured velocity dispersion profile. Bottom: velocity dispersion profile of the spherical model and of an oblate (prolate) ellipsoid with minor (major) axis parallel to the line of sight and axis ratio 0.8.

(A color version of this figure is available in the online journal.)

(observed) projected mass within the Einstein radius? We use the axisymmetric Jeans equation to address this question as well. We take our best-fit spherical model and modify it into an oblate (prolate) ellipsoid with the axis ratio of both the light and mass distribution fixed at 0.8, orienting L_z along the line of sight. The line-of-sight velocity dispersion profile for isotropic orbits in the oblate and prolate case is also plotted in Figure 17. The spread relative to the spherical case is somewhat larger than the uncertainties. To make sure that our assumption of spherical symmetry does not alter the measurements presented in this paper we recalculate the inference of the key model parameters by inflating the error bars on the velocity dispersion measurements by a factor 1.5, matching the scatter introduced by the unknown line-of-sight oblateness or prolateness of the lens. None of the results change appreciably. The lens modeling does not depend on assumptions on the line-of-sight mass distribution, and so in this regard our results are robust.

REFERENCES

Abadi, M. G., Navarro, J. F., Fardal, M., Babul, A., & Steinmetz, M. 2010, MNRAS, 407, 435
Auger, M. W., Treu, T., Bolton, A. S., et al. 2009, ApJ, 705, 1099
Auger, M. W., Treu, T., Bolton, A. S., et al. 2010a, ApJ, 724, 511
Auger, M. W., Treu, T., Gavazzi, R., et al. 2010b, ApJ, 721, L163
Barnabè, M., Czoske, O., Koopmans, L. V. E., Treu, T., & Bolton, A. S. 2011, MNRAS, 415, 2215
Barth, A. J., Ho, L. C., & Sargent, W. L. W. 2002, AJ, 124, 2607
Bell, E. F., & de Jong, R. S. 2001, ApJ, 550, 212
Benítez, N. 2000, ApJ, 536, 571
Bennert, V. N., Auger, M. W., Treu, T., Woo, J.-H., & Malkan, M. A. 2011, ApJ, 726, 59
Bertin, E., Mellier, Y., Radovich, M., et al. 2002, in ASP Conf. Ser. 281, Astronomical Data Analysis Software and Systems XI, ed. D. A. Bohlender, D. Durand, & T. H. Handley (San Francisco, CA: ASP), 228
Bertin, G., Bertola, F., Buson, L. M., et al. 1994, A&A, 292, 381
Binney, J., & Tremaine, S. 2008, in Galactic Dynamics, ed. J. Binney & S. Tremaine (2nd ed.; Princeton, NJ: Princeton Univ. Press), 357
Blumenthal, G. R., Faber, S. M., Flores, R., & Primack, J. R. 1986, ApJ, 301, 27
Bolton, A. S., Burles, S., Schlegel, D. J., Eisenstein, D. J., & Brinkmann, J. 2004, AJ, 127, 1860
Brewer, B. J., Dutton, A. A., Treu, T., et al. 2012, MNRAS, in press (arXiv:1201.1677)
Bruzual, G., & Charlot, S. 2003, MNRAS, 344, 1000
Cappellari, M., Bacon, R., Bureau, M., et al. 2006, MNRAS, 366, 1126
Cappellari, M., McDermid, R. M., Alatalo, K., et al. 2012, Nature, 484, 485
Cardelli, J. A., Clayton, G. C., & Mathis, J. S. 1989, ApJ, 345, 245
Ciotti, L., Ostriker, J. P., & Proga, D. 2010, ApJ, 717, 708
Coe, D., Benítez, N., Sánchez, S. F., et al. 2006, AJ, 132, 926
Daddi, E., Renzini, A., Pirzkal, N., et al. 2005, ApJ, 626, 680
Djorgovski, S., & Davis, M. 1987, ApJ, 313, 59
Dressler, A., Lynden-Bell, D., Burstein, D., et al. 1987, ApJ, 313, 42
Duffy, A. R., Schaye, J., Kay, S. T., et al. 2010, MNRAS, 405, 2161
Dutton, A. A., Brewer, B. J., Marshall, P. J., et al. 2011, MNRAS, 417, 1621
Ferrarese, L., & Merritt, D. 2000, ApJ, 539, L9
Ferreras, I., Saha, P., Leier, D., Courbin, F., & Falco, E. E. 2010, MNRAS, 409, L30
Franx, M., van Gorkom, J. H., & de Zeeuw, T. 1994, ApJ, 436, 642
Fruchter, A., Sosey, M., Hack, W., et al. 2009, The MultiDrizzle Handbook, Version 3.0 (Baltimore, MD: STScI)
Gavazzi, R., Treu, T., Koopmans, L. V. E., et al. 2008, ApJ, 677, 1046
Gavazzi, R., Treu, T., Rhodes, J. D., et al. 2007, ApJ, 667, 176
Gebhardt, K., Bender, R., Bower, G., et al. 2000, ApJ, 539, L13
Gerhard, O., Kronawitter, A., Saglia, R. P., & Bender, R. 2001, AJ, 121, 1936
Gnedin, O. Y., Kravtsov, A. V., Klypin, A. A., & Nagai, D. 2004, ApJ, 616, 16
Grillo, C. 2012, ApJ, 747, L15
Grillo, C., Gobat, R., Lombardi, M., & Rosati, P. 2009, A&A, 501, 461
Gustafsson, M., Fairbairn, M., & Sommer-Larsen, J. 2006, Phys. Rev. D, 74, 123522
Haehnelt, M. G., & Kauffmann, G. 2000, MNRAS, 318, L35
Hernquist, L. 1992, ApJ, 400, 460
Hilbert, S., White, S. D. M., Hartlap, J., & Schneider, P. 2007, MNRAS, 382, 121
Hopkins, P. F., Bundy, K., Hernquist, L., Wuyts, S., & Cox, T. J. 2010, MNRAS, 401, 1099
Hopkins, P. F., Bundy, K., Murray, N., et al. 2009a, MNRAS, 398, 898
Hopkins, P. F., Hernquist, L., Cox, T. J., Keres, D., & Wuyts, S. 2009b, ApJ, 691, 1424
Hyde, J. B., & Bernardi, M. 2009, MNRAS, 394, 1978
Koopmans, L. V. E., Bolton, A., Treu, T., et al. 2009, ApJ, 703, L51
Koopmans, L. V. E., & Treu, T. 2003, ApJ, 583, 606
Koopmans, L. V. E., Treu, T., Bolton, A. S., Burles, S., & Moustakas, L. A. 2006, ApJ, 649, 599
Koopmans, L. V. E., Treu, T., Fassnacht, C. D., Blandford, R. D., & Surpi, G. 2003, ApJ, 599, 70
Kormendy, J., & Sanders, D. B. 1992, ApJ, 390, L53
Macciò, A. V., Dutton, A. A., & van den Bosch, F. C. 2008, MNRAS, 391, 1940
Marconi, A., & Hunt, L. K. 2003, ApJ, 589, L21

Merritt, D. 1985, AJ, 90, 1027
Napolitano, N. R., Romanowsky, A. J., & Tortora, C. 2010, MNRAS, 405, 2351
Navarro, J. F., Frenk, C. S., & White, S. D. M. 1997, ApJ, 490, 493
Newman, A. B., Ellis, R. S., Bundy, K., & Treu, T. 2012, ApJ, 746, 162
Newman, A. B., Ellis, R. S., Treu, T., & Bundy, K. 2010, ApJ, 717, L103
Newman, A. B., Treu, T., Ellis, R. S., et al. 2009, ApJ, 706, 1078
Nipoti, C., Treu, T., Auger, M. W., & Bolton, A. S. 2009, ApJ, 706, L86
Oser, L., Naab, T., Ostriker, J. P., & Johansson, P. H. 2012, ApJ, 744, 63
Osipkov, L. P. 1979, Sov. Astron. Lett., 5, 42
Padilla, N. D., & Strauss, M. A. 2008, MNRAS, 388, 1321
Peng, C. Y. 2007, ApJ, 671, 1098
Sand, D. J., Treu, T., Ellis, R. S., Smith, G. P., & Kneib, J.-P. 2008, ApJ, 674, 711
Schaye, J., Dalla Vecchia, C., Booth, C. M., et al. 2010, MNRAS, 402, 1536
Shen, S., Mo, H. J., White, S. D. M., et al. 2003, MNRAS, 343, 978
Shier, L. M., & Fischer, J. 1998, ApJ, 497, 163
Spiniello, C., Koopmans, L. V. E., Trager, S. C., Czoske, O., & Treu, T. 2011, MNRAS, 417, 3000
Suyu, S. H., Hensel, S. W., McKean, J. P., et al. 2012, ApJ, 750, 10
Suyu, S. H., Marshall, P. J., Auger, M. W., et al. 2010, ApJ, 711, 201
Suyu, S. H., Marshall, P. J., Blandford, R. D., et al. 2009, ApJ, 691, 277
Treu, T. 2010, ARA&A, 48, 87
Treu, T., Auger, M. W., Koopmans, L. V. E., et al. 2010, ApJ, 709, 1195
Treu, T., Gavazzi, R., Gorecki, A., et al. 2009, ApJ, 690, 670
Treu, T., & Koopmans, L. V. E. 2004, ApJ, 611, 739
Trujillo, I., Feulner, G., Goranova, Y., et al. 2006, MNRAS, 373, L36
van der Wel, A., Holden, B. P., Zirm, A. W., et al. 2008, ApJ, 688, 48
van Dokkum, P. G., & Conroy, C. 2010, Nature, 468, 940
van Dokkum, P. G., & Conroy, C. 2011, ApJ, 735, L13
van Dokkum, P. G., Franx, M., Kriek, M., et al. 2008, ApJ, 677, L5
Vegetti, S., Koopmans, L. V. E., Bolton, A., Treu, T., & Gavazzi, R. 2010, MNRAS, 408, 1969